





















Earliest Galaxy Evolution in the CANUCS+Technicolor fields: Galaxy Properties at $z \sim 10 - 16$ seen with the Full NIRC*am* Medium and Broad Band Filters

YOSHIHISA ASADA ^{1,2,3} CHRIS J. WILLOTT ⁴ ADAM MUZZIN ⁵ MARUŠA BRADAČ ^{6,7} GABRIEL BRAMMER ^{8,9}
GUILLAUME DESPREZ ¹⁰ KARTHEIK G. IYER ¹¹ DANILO MARCHESINI ¹² NICHOLAS S. MARTIS ⁶ GAËL NOIROT ¹³
GHASSAN T. E. SARROUH ⁵ MARCIN SAWICKI ¹⁴ SUNNA WITHERS ⁵ SEIJI FUJIMOTO ^{2,3} GIORDANO FELICIONI ⁶
ILIAS GOOVAERTS ¹³ JON JUDEŽ ⁶ NAADIYAH JAGGA ⁵ MAYA MERCHANT⁹ ROSA M. MÉRIDA ¹⁴ AND
LUKE ROBBINS ¹⁵

¹Waseda Research Institute for Science and Engineering, Faculty of Science and Engineering, Waseda University,
3-4-1 Okubo, Shinjuku, Tokyo 169-8555, Japan

²Dunlap Institute for Astronomy and Astrophysics, 50 St. George Street, Toronto, Ontario M5S 3H4, Canada

³David A. Dunlap Department of Astronomy and Astrophysics, University of Toronto,
50 St. George Street, Toronto, Ontario M5S 3H4, Canada

⁴NRC Herzberg, 5071 West Saanich Rd, Victoria, BC V9E 2E7, Canada

⁵Department of Physics and Astronomy, York University, 4700 Keele St., Toronto, Ontario M3J 1P3, Canada

⁶Faculty of Mathematics and Physics, University of Ljubljana, Jadranska ulica 19, SI-1000 Ljubljana, Slovenia

⁷Department of Physics and Astronomy, University of California Davis, 1 Shields Avenue, Davis, CA 95616, USA

⁸Cosmic Dawn Center (DAWN), Denmark

⁹Niels Bohr Institute, University of Copenhagen, Jagtvej 128, DK-2200 Copenhagen N, Denmark

¹⁰Kapteyn Astronomical Institute, University of Groningen, P.O. Box 800, 9700AV Groningen, The Netherlands

¹¹Columbia Astrophysics Laboratory, Columbia University, 550 West 120th Street, New York, NY 10027, USA

¹²Department of Physics & Astronomy, Tufts University, MA 02155, USA

¹³Space Telescope Science Institute, 3700 San Martin Drive, Baltimore, Maryland 21218, USA

¹⁴Department of Astronomy and Physics and Institute for Computational Astrophysics, Saint Mary's University, 923 Robie Street,
Halifax, Nova Scotia B3H 3C3, Canada

¹⁵Department of Physics & Astronomy, Tufts University, 574 Boston Avenue, Suite 304, Medford, MA 02155, USA

Submitted to ApJ

ABSTRACT

We present a sample of $z_{\text{phot}} \sim 10 - 16$ galaxies by exploiting one of the richest JWST NIRC*am* imaging data, taken in the CANUCS survey in Cycle 1 and the Technicolor (TEC) survey in Cycle 2. The combination of the CANUCS+TEC provides multi-epoch, deep NIRC*am* images in all medium bands (MBs) and broad bands (BBs) onboard NIRC*am* (22 filters in total), over $\sim 23 \text{ arcmin}^2$ in three independent lines of sight. We select high- z galaxy candidates based on photometric redshifts, and obtain eight candidates at $z \sim 10 - 16$, including a very robust candidate at $z \sim 15.4$. The ultraviolet (UV) luminosity function (LF) from our sample is consistent with previous JWST studies showing a scatter of ~ 0.6 dex across the literature, marking the significance of the field-to-field variance in interpreting galaxy abundance measurements at $z > 10$. We find that the UV LF moderately evolves at $z > 10$, and the LF normalization and the luminosity density decline by a factor of ~ 7 from $z \sim 11$ to $z \sim 15$, indicating less steep evolution than $z < 11$. We highlight the importance of MB filters, not only to minimize the contamination by low- z interlopers but also to maximize the completeness. In particular, faint and less blue galaxies could be missed when the sample is built solely on BB data. The contamination and incompleteness of BB-only selected samples can bias our views of earliest galaxy evolution at $z > 10$, including the UV LF by ~ 0.6 dex, the size-magnitude relation by ~ 0.6 dex, and the UV slope-magnitude relation by $\Delta\beta_{\text{UV}} \sim -0.3$.

Keywords: Galaxies (573) — Galaxy formation (595) — Galaxy evolution (594) — Luminosity function (942) — High-redshift galaxies (734)

1. INTRODUCTION

Finding and characterizing the earliest galaxies is one of the major quests in modern astronomy. The James Webb Space Telescope (JWST) has made a breakthrough in this field with its capability of finding $z \gtrsim 10$ galaxies. Numerous $z > 10$ galaxy candidates have been identified with NIRCam imaging (e.g., Y. Harikane et al. 2023; P. G. Pérez-González et al. 2023; N. J. Adams et al. 2024; K. N. Hainline et al. 2024; C. J. Willott et al. 2024; M. Castellano et al. 2025; P. G. Pérez-González et al. 2025). The statistical search for high- z galaxy candidates with NIRCam imaging is in particular essential to probe the earliest galaxy evolution. Tracking the early evolution of galaxy number density, e.g., the UV luminosity function (LF), directly unveils how first galaxies have emerged from the initial matter perturbation and how they have grown with baryon accretion in dark matter halos (e.g., R. J. Bouwens et al. 2021; Y. Harikane et al. 2022).

Various NIRCam imaging surveys have been carried out in the first three years of JWST observation, most of which employed the standard Broad-band (BB) filter configurations. This has been a good strategy as BB filters are wide in wavelength coverage, offering good spectral energy distribution (SED) coverage but also facilitating deep photometry with efficient integration times. Given that the Lyman break feature is strong and does not require high spectral resolution, the BB approach in the initial years of JWST has been sensible and highly efficient at discovering $z > 10$ galaxy candidates. Thus far, many $z_{\text{phot}} \gtrsim 10$ galaxy samples are built relying on the BB-only photometry data, including galaxy candidates even up to $z_{\text{phot}} \sim 25$ (e.g., M. Castellano et al. 2025; P. G. Pérez-González et al. 2025). However, the selection of high- z galaxies with BB-only data needs to be treated with caution, because the BB photometry spectral energy distributions (SEDs) of interlopers at lower- z with strong emission lines combined with a Balmer break or a red, dusty continuum can mimic the high- z galaxy SED and contaminate the high- z galaxy sample. Perhaps the most prominent example of this is the galaxy CEERS-9331, which was originally identified as a bright $z \sim 16$ galaxy candidate by several independent authors based on the seven BB filters + F410M photometric data (e.g., C. T. Donnan et al. 2023; Y. Harikane et al. 2023), but subsequent NIRSpect observation confirmed it as a dusty extreme emission line galaxy at $z = 4.9$ (P. Arrabal Haro et al. 2023).

Particularly at $z > 9.5$, all strong rest-frame optical emission lines are redshifted beyond NIRCam filter coverage, and the Lyman- α break at $\lambda_{\text{rest}} = 1216 \text{ \AA}$ is the only signature to identify $z > 9.5$ galaxy candidates from photometry. The combination of NIRCam Medium-band (MB) and BB filter observations is one way to minimize contamination when building robust $z > 9.5$ galaxy samples (e.g., N. J. Adams et al. 2025). NIRCam MB observations have successfully shown that they can identify strong emission lines from the flux excess in MB filters (e.g., S. Withers et al. 2023; G. T. E. Sarrouh et al. 2024; K. A. Suess et al. 2024; N. Martis et al. 2025) and therefore they are extremely efficient at identifying low- z strong line emitters that contaminate high- z candidates such as in P. Arrabal Haro et al. (2023). MB+BB observations also allow us to precisely locate the sharp break in the continuum at the Lyman break. Thus MB+BB filter observations should unambiguously distinguish low- z interlopers with strong emission lines vs real high- z galaxies with sharp continuum drop-outs.

Not only can MBs efficiently rule out interlopers, they can also help properly classify real candidates previously considered more likely to be low- z contaminants with BB-only data. One good showcase of this is GS-z14-0 at $z_{\text{spec}} = 14.18$ (S. Carniani et al. 2025). GS-z14-0 was originally identified from NIRCam BB imaging observations in Cycle 1, but it was thought to be at $z \sim 3.5$ with the BB-only data (C. C. Williams et al. 2024). After obtaining MB observations in Cycle 2, GS-z14-0 was identified as a secure $z \sim 14$ galaxy candidate (B. Robertson et al. 2024), and the subsequent spectroscopic follow-up observation proved it to be at $z_{\text{spec}} = 14.18$ (S. Carniani et al. 2024, 2025).

Specifically, the combination of F140M, F150W, and F162M is powerful in selecting $z \sim 10 - 13$ galaxies, and that of F182M, F200W, and F210M in selecting $z \sim 13 - 16$ galaxies, as they simultaneously cover the Lyman break wavelength range with two MBs and one BB overlapping each other, and they can locate the sharp drop-out from photometry (or strong emission line excess for low- z interlopers). B. Robertson et al. (2024) exploited a deep MB+BB NIRCam survey program, the JADES Origins Field (JOF; D. J. Eisenstein et al. 2023), to derive the galaxy UV LF at $z > 9.5$ based on 14 NIRCam filter images (seven MBs and seven BBs) in a very deep, single NIRCam pointing. As pointed out by B. Robertson et al. (2024), galaxy abundance mea-

measurements in such a small area are affected by cosmic variance, and it is necessary to enlarge the survey volume for $z > 10$ galaxies with a comprehensive set of MB+BB filters.

In this paper, we present UV LF measurements at $z > 9.5$ using data from the CANadian NIRISS Unbiased Cluster Survey (CANUCS; GTO-1208, PI: Willott; C. J. Willott et al. 2022) in Cycle 1 and the JWST in Technicolor program (TEC; GO-3362, PI: Muzzin) in Cycle 2. Combining CANUCS+TEC provides the full set of NIRCcam BB+MB filter observations (+ two narrow-band filters) in three independent NIRCcam pointings. Observing three independent sight lines with the rich MB+BB filters adds an invaluable constraint on the early UV LF evolution, by building a new, very clean $z > 10$ galaxy sample in addition to the previous work in the JOF. We also explore the potential bias due to low- z interloper contamination in BB-only data selection of $z \gtrsim 10$ galaxies, by comparing our main $z \gtrsim 10$ candidates built from MB+BB observations and those from a degraded BB-only photometry catalog.

The paper is structured as follows. Sec. 2 describes the imaging data and data processing we use in this work. Sec. 3 presents the sample selection of high- z galaxies and the completeness simulation of our selection. Sec. 4 gives the main result of this paper, including the UV LF at $z > 9.5$ and the redshift evolution of the UV luminosity density. Sec. 5 is the discussion focusing on what can affect measurements of high- z galaxy abundance in JWST surveys, including cosmic variance and low- z interlopers in BB-only data selections. The section also discusses the potential bias by inclusion of low- z interlopers with BB-only data in various aspects of galaxy properties at $z > 10$ and future prospects from scheduled JWST Cycle 4 observations. Sec. 6 finally provides the summary of the paper. Throughout the paper, we assume a flat Λ CDM cosmology with $\Omega_m = 0.3$, $\Omega_\Lambda = 0.7$, and $H_0 = 70 \text{ km s}^{-1} \text{ Mpc}^{-1}$, and all magnitudes are quoted in the AB system (J. B. Oke & J. E. Gunn 1983).

2. DATA

2.1. Imaging Data and Photometry

We use JWST/NIRCcam imaging data from CANUCS in Cycle 1 and TEC in Cycle 2 of the three NIRCcam flanking fields (NCFs). The overall survey description and full details of the imaging reduction are presented in G. T. E. Sarrouh et al. (2025, SA25 hereafter). Combining the multi-epoch two surveys, a total of three NIRCcam pointings are observed with all NIRCcam BB and

MB filters¹, in addition to two narrow-band filters of F164N and F187N. Each NIRCcam pointing is an associated flanking field of the strong lensing cluster field (MACS 0416, MACS 1149, and A 370), and we refer to these flanking fields as NCF fields. As we only use the flanking fields, the effect of gravitational lensing is negligibly small in this work. Table 1 presents the limiting magnitudes of all available NIRCcam filters in each field. The table also includes the information about the observing cycle (Cycle 1 by CANUCS program or Cycle 2 by TEC program).

We also utilize HST optical imaging observations in F435W, F606W, and F814W filters on Advanced Camera for Surveys (ACS), taken in previous observations by the Hubble Frontier Fields Parallels program (J. M. Lotz et al. 2017). The HST/ACS footprints partially overlap with the NIRCcam area (typically $\sim 50\%$ of NIRCcam field-of-views), so we use HST/ACS photometry when available for photometric redshift computation (Sec. 2.2), but do not adopt S/N cuts in HST/ACS filter images in the sample selection. There are also several HST Wide Field Camera 3 infra-red filter images available in these fields, but we do not use them in this work, given the wavelength overlap with NIRCcam and the superior quality of NIRCcam images in resolution and sensitivity.

We exploit the background-subtracted images and the source detection catalogs given by SA25, but we perform custom photometry to maximize the signal-to-noise ratio (S/N) for faint, small sources barely resolved with NIRCcam imaging. Namely, at the position of each detected source, we perform fixed aperture photometry with a $0''.16$ -diameter aperture on the background-subtracted images that have not been convolved to a common PSF. We correct the aperture photometry in each filter based on the PSF encircled energies (EEs) of the filter, since the galaxies are small. The photometry is then corrected for Galactic extinction with the E. L. Fitzpatrick (1999) extinction curve assuming $R_V = 3.1$, to obtain the color (i.e., SEDs) of each detected source. The total flux of each source is estimated by scaling the SED with the Kron-to-aperture-corrected flux ratios in the F277W image.

2.2. Photometric Redshift

We select high- z galaxies using photometric redshifts (photo- z) in this work. The photo- z is estimated using the template-fitting code EAzy-py (G. B. Brammer et al. 2008) under almost the same configuration as in

¹ except for the MACS 1149 flanking field: F162M and F250M are missing due to a program definition error

Table 1. Summary of JWST/NIRCam and HST/ACS observations in CANUCS+Technicolor fields.

Filter (Obs. Cycle)	MACS 0416	MACS 1149	A 370
F070W (Cy. 2)	29.74	29.69	29.65
F090W (Cy. 1)	30.20	30.16	30.09
F115W (Cy. 1)	30.23	30.17	30.05
F140M (Cy. 1)	29.51	29.34	29.28
F150W (Cy. 1)	30.35	30.41	30.18
F162M (Cy. 1)	29.53	...	29.43
F164N (Cy. 2)	27.38	27.40	27.34
F182M (Cy. 1)	30.02	30.01	29.90
F187N (Cy. 2)	27.37	27.47	27.44
F200W (Cy. 2)	30.02	29.99	29.90
F210M (Cy. 1)	29.90	29.84	29.79
F250M (Cy. 1)	29.30	...	29.11
F277W (Cy. 1)	30.60	30.65	30.49
F300M (Cy. 1)	29.71	29.58	29.52
F335M (Cy. 1)	29.97	29.93	29.84
F356W (Cy. 2)	30.13	30.06	30.03
F360M (Cy. 1)	29.85	29.85	29.76
F410M (Cy. 1)	29.67	29.68	29.57
F430M (Cy. 2)	28.91	28.90	28.91
F444W (Cy. 1)	29.91	29.82	29.75
F460M (Cy. 2)	28.55	28.48	28.50
F480M (Cy. 2)	28.53	28.47	28.51
F435W	30.09	30.01	30.05
F606W	29.64	29.59	29.80
F814W	29.73	29.19	29.63
Area (arcmin ²) ^a	7.57	7.88	7.87

Notes. For each filter, the 3-sigma limiting magnitudes (in ABmag) are quoted. The limiting magnitudes are measured in 0''.16-diameter aperture, by randomly distributing empty apertures in the background sky region of each image (without PSF-convolution) and performing aperture correction based on the PSF EEs.

^aThe unmasked sky area from completeness simulations is quoted.

SA25. A total of 15 galaxy template spectra are used in the fit, 12 of which are from FSPS (C. Conroy & J. E. Gunn 2010) and the other three are custom templates based on R. L. Larson et al. (2023, see SA25 for details of the modification). No magnitude-based redshift prior is assumed, while systematic uncertainties of 5 % of observed fluxes are added to the flux error budget in quadrature. The galaxy template spectra are corrected for the inter-galactic medium (IGM) absorption following the prescription by Y. Asada et al. (2025), which

takes into account the effect of increasing Ly α damping-wing absorption at $z > 7$, on top of the canonical IGM transmission curve (A. K. Inoue et al. 2014). We stress that the use of the IGM modeling by Y. Asada et al. (2025) is expected to resolve the photo- z overestimation at $z \gtrsim 7$, which has been commonly seen in previous works just using classical IGM prescriptions, and this reduces a systematic uncertainty with regard to the redshift and absolute magnitude estimation of high- z galaxies. Under this configuration, we compute the photo- z probability function (PDZ) of each source from $z = 0$ to 20, and obtain the best photo- z estimation (z_{ml}) based on the peak of the PDZ.

3. SAMPLE SELECTION

We present the high- z galaxy sample as defined at $z > 9.5$ in this work. To minimize the low- z interlopers into the sample, we adopt the following selection criteria:

$$\begin{aligned}
 S/N_{\text{Blue}} &< 3, \\
 S/N_{\text{F277W}} &> 9, \\
 \int_0^7 P(z) dz &< 0.1, \\
 9.5 &< z_{\text{ml}} < 16,
 \end{aligned} \tag{1}$$

where $S/N_{\text{Blue}} < 3$ means the signal-to-noise ratio (S/N) in bluer filters (F070W, F090W, and F115W) are all less than 3. Requiring S/Ns smaller than 3 in three independent filters would remove ~ 1 % of real sources by the random errors. If we required S/Ns smaller than 2 instead, we would miss ~ 14 % of real candidates due to the random noise. The limit of low- z solution probability is applied to select only high- z sources with high confidence level and remove possible low- z interlopers that have double-peaked $P(z)$. We also adopt the redshift upper limit of 16 to remove any spurious NIRCam long wave (LW)-only sources: this is because the relatively large wavelength coverage gap between NIRCam short-wave (SW) filters and LW filters, unmasked bad pixels in the LW detectors, broader PSF size at longer wavelength, or the combination of them can easily produce fake high- z candidates that are detected only in NIRCam LW filters. The motivation of this work is to provide the cleanest sample of $z > 9.5$ galaxies possible, relying on the rich NIRCam MB+BB observations that are capable to robustly capture the Lyman break, thus we limit the redshift up to $z < 16$ where the dropout can still be detected with F200W and F210M on the SW detectors.

A total of eight galaxies are selected by the criteria (equation 1), and we use them for the subsequent luminosity function analysis. Three of them (CANUCS ID:

Table 2. High-redshift galaxy candidates in CANUCS+Technicolor fields.

Name	R.A.	Decl.	z_{ml}	M_{UV}	β_{UV}	r_{eff} [pc]	$P(z < 7)$
(1)	(2)	(3)	(4)	(5)	(6)	(7)	(8)
CANUCS-5223684	177.414290	22.32748	$9.65^{+0.32}_{-0.35}$	-18.37	-2.14 ± 0.22	17.1 ± 2.3	4.96e-04
CANUCS-3209488	64.169709	-24.10793	$9.69^{+0.24}_{-0.36}$	-19.23	-1.88 ± 0.27	487.9 ± 27.3^a	2.76e-09
CANUCS-2215881	40.056129	-1.61568	$9.78^{+0.13}_{-0.43}$	-19.09	-2.20 ± 0.14	109.8 ± 83.3	8.00e-11
CANUCS-5221204	177.386651	22.30266	$10.15^{+0.02}_{-1.42}$	-18.89	-2.67 ± 0.37	207.6 ± 91.1	2.17e-03
CANUCS-2219868	40.032579	-1.60055	$10.32^{+0.15}_{-0.26}$	-19.52	-2.33 ± 0.16	112.4 ± 32.6^b	1.66e-04
CANUCS-5208401	177.404008	22.32253	$10.69^{+0.33}_{-0.38}$	-18.75	-1.93 ± 0.30	15.9 ± 2.1	6.52e-02
CANUCS-5203757	177.408240	22.28612	$11.23^{+0.14}_{-0.10}$	-19.77	-2.18 ± 0.07	15.3 ± 2.0	9.92e-19
CANUCS-3214552	64.133557	-24.07987	$15.43^{+0.26}_{-0.57}$	-18.98	-1.80 ± 0.34	29.2 ± 1.3	5.05e-03

(1) Source IDs in the CANUCS catalog by SA25. (2) Right Ascension in J2000. (3) Declination in J2000. (4) Best photo- z estimations. Uncertainties are from the 16th- to 84th-percentile range of $P(z)$. (5) Absolute rest UV magnitudes. (6) UV slopes measured from NIRCcam photometry. (7) The intrinsic, PSF-deconvolved effective radii r_{eff} in the NIRCcam F277W image. (8) Low- z solution probabilities.

^aThe source appears to have two components in the NIRCcam image, but fails to fit with two Sérsic components and results of fitting a single component are quoted.

^bFitted with two Sérsic components, and the size of the main clump is quoted.

2215881, 2219868, and 5203757) were reported in our previous work (C. J. Willott et al. 2024) in the same fields, but the rest are new. We note that the previous work only used CANUCS Cycle 1 observations and utilized smaller number of NIRCcam filters. The five new sources were not included in the previous work mostly because of their non-negligible low- z solution probability, which becomes negligible with the new NIRCcam observations from the TEC survey in Cycle 2. On the other hand, two sources included in the previous work are not selected in this work, and they are both due to low S/N in F277W. For each high- z candidate, we also measure the rest-UV beta slope β_{UV} and the effective radius r_{eff} in the NIRCcam F277W image. For β_{UV} measurements, we fit a pure power law $f_{\lambda} \propto \lambda^{\beta}$ to the NIRCcam photometry that corresponds to $\lambda_{\text{rest}} < 3000$ Å and covers only the filters redward of the Ly α transition. Thanks to the extensive NIRCcam observations, the β_{UV} measurements are based on 5 to 9 NIRCcam data points. For r_{eff} measurements, we perform forward modeling assuming the Sérsic light profile with *Galfit* (C. Y. Peng et al. 2010). We assume a single Sérsic component by default, but we adopt two-component fitting when the high-resolution NIRCcam images show two clumps (CANUCS-2219868). Table 2 lists the eight candidates in this work. The eight galaxies are found at $z \sim 9.5$ to $z \sim 15$, and they are typically faint, moderately blue, and compact galaxies. We note that the gravitational lens magnifications of the eight galaxies are negligibly small ($\langle \mu \rangle = 1.02$).

3.1. A remarkable $z > 15$ galaxy candidate: CANUCS-3214552

The highest redshift candidate among the sample is CANUCS-3214552, whose best photo- z estimate is $z_{\text{ml}} = 15.43^{+0.26}_{-0.57}$ with a negligible low- z possibility ($P(z < 7) = 5.1 \times 10^{-3}$; Figure 1). The galaxy is faint and relatively red in UV ($M_{\text{UV}} = -19.0$ mag and $\beta_{\text{UV}} = -1.8$), and the sharp dropout is captured between the F182M+F200W and F210M filters. Together with the flat SED at longer wavelengths, the sharp break in the narrow wavelength range between F182M and F210M and the dropout in F200W strongly support the $z = 15.4$ solution over the low- z ($z = 4$) solution (the blue solid curve in the bottom right panel of Figure 1). Indeed, this source would have a non-negligible secondary low- z peak in the PDZ if only the standard set of NIRCcam eight filters (seven BBs + F410M) were available (the dashed curve in the panel) and would not be selected as a secure high- z candidate.

Moreover, the multi-epoch observations confirmed there is no evidence for variability. Several studies have shown that some types of supernovae (SNe) at $2 < z < 5$ have strong breaks around rest 4000 Å wavelength, which can mimic the color of highest- z LBGs (e.g., H. Yan et al. 2023; C. DeCoursey et al. 2025). C. DeCoursey et al. (2025) suggested that a high fraction of point-like, $z \sim 16$ candidates could be SNe at $z \sim 4$. However in the case of CANUCS-3214552, the galaxy was observed in Cycle 1 and Cycle 2 with one year sepa-

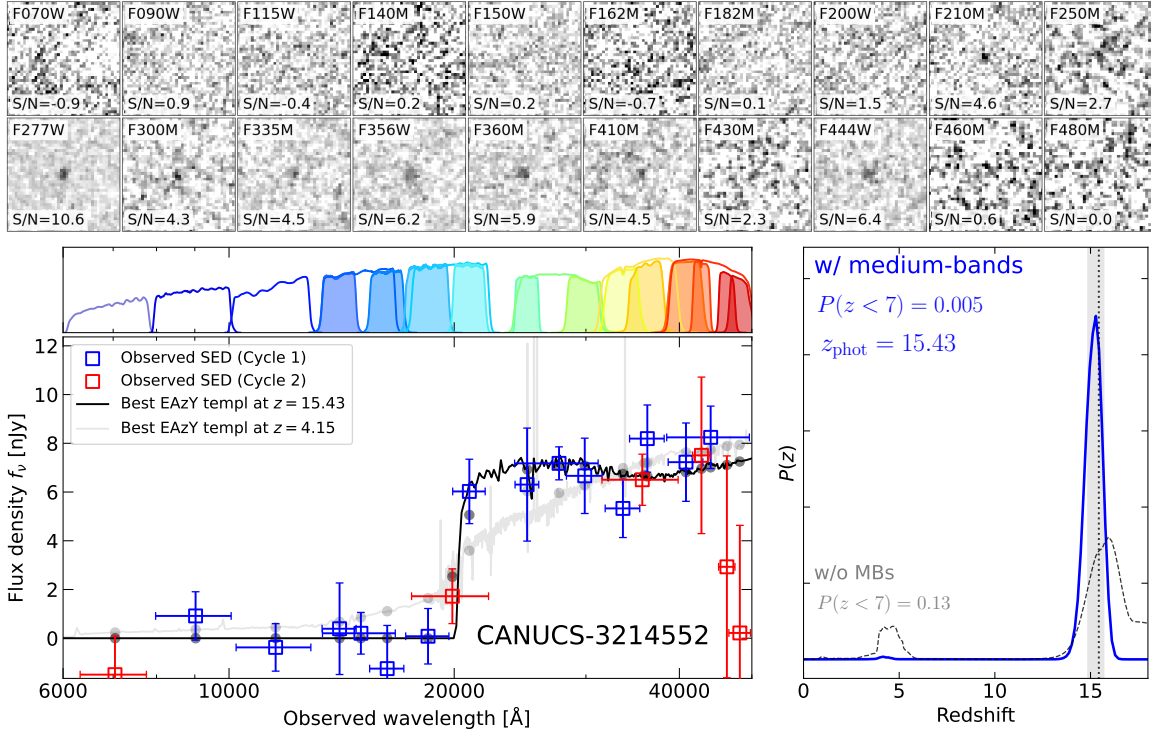


Figure 1. The highest redshift candidate of CANUCS-3214552 at $z_{\text{phot}} \sim 15.4$. *Top:* cutouts of the source in all NIRCам filter images, except for the two narrow band filters. Cutouts are $1''6$ on the side. *Bottom:* the SED and the PDZ of CANUCS-3214552. The SED shows a clear dropout between F210M and F200W, and the sharp drop between this narrow wavelength range strongly supports the high- z solution template (black solid curve in the bottom left panel) and results in negligible low- z probability (blue curve in the bottom right panel). There is no variability between Cycle 1 and Cycle 2 observation with 1 year separation (blue and red squares in bottom left), which rules out the possibility of $z \sim 4$ SN contamination. If MB data were not available, the SED could also be fit by a low- z solution (gray curve in bottom left) and the PDZ would have a non-negligible secondary peak at $z \sim 4$ (gray dashed line in bottom right). Only multiple-epoch rich MB+BB observations can secure this galaxy as a very robust $z \sim 15$ galaxy candidate.

ration and the NIRCам photometry agrees well between the two epochs (e.g., F335M and F360M taken in Cycle 1 vs. F356W taken in Cycle 2).

CANUCS-3214552 is thus one of the most reliable high- z galaxy candidates at $z > 15$, which could have been secured only with the multi-epoch, full NIRCам MB+BB observations. The galaxy shows a relatively red rest-UV color, in contrast to recent reports of very blue colors for the most of faint highest- z galaxies (e.g., F. Cullen et al. 2024), and it could suggest the galaxy represents a galaxy population that has been missed in previous surveys using the standard NIRCам BB configuration. We provide a detailed discussion on this point later (Sec. 5.3.2).

3.2. Completeness simulation

A luminosity function estimation requires computation of the effective volume that has been searched, taking account of the effect of detection and selection completeness. Our selection criteria (equation 1) are fully automated and we do not apply additional cuts based

on visual inspection. Thus, we can estimate the completeness by inserting simulated sources into our data and repeating the detection and selection procedure to measure the recovered fraction. We follow the completeness simulation prescription of C. J. Willott et al. (2024) with a few modifications.

For the simulated galaxy size distribution, C. J. Willott et al. (2024) used a redshift-dependent size- M_{UV} relationship derived from a photometric-redshift-selected sample of high- z galaxies from T. Morishita et al. (2024). As we show in Sec. 5.3.1, the $z > 9.5$ galaxies from the current study plus those from the JOF that also includes MB photometry (B. Robertson et al. 2024) have sizes considerably smaller (median offset 0.6 dex) than that of the T. Morishita et al. (2024) relationship. Therefore, we offset the T. Morishita et al. (2024) relationship by 0.6 dex for the size distribution of the simulated galaxies.

The SEDs of the simulated galaxies incorporate the updated Larson templates and IGM absorption used in deriving photometric redshifts (Sec. 2.2), as described

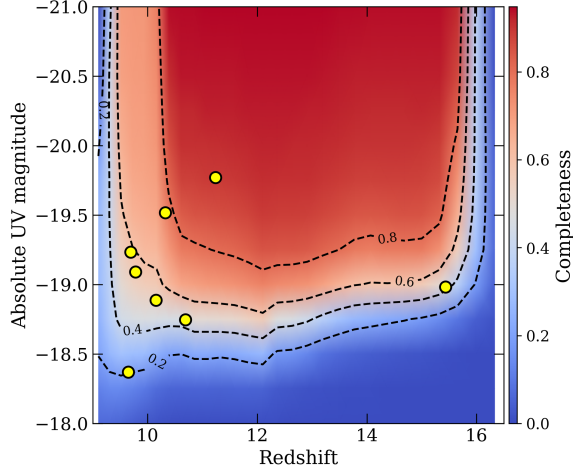


Figure 2. High- z galaxy selection completeness in the absolute UV magnitude vs redshift plane. Yellow points present our main $z > 9.5$ galaxy sample selected by criteria (1). Our selection is 50 % complete down to $M_{\text{UV}} \sim -18.7$ mag over the full redshift range of $10 \lesssim z \lesssim 16$. Though, only one galaxy is found at $z > 12$ whereas seven are found at $z < 12$, which indicates redshift evolution of the UV LF across this redshift range.

in detail in SA25. We adopt a set of 4 template spectra with a range of stellar age, dust attenuation and emission line strength that gives a F200W-F277W color distribution comparable to that of our sample.

A grid of M_{UV} and redshift covering the range of this study was set up. At each point in this plane, simulated galaxies were randomly inserted into all the NIRCcam images of the three fields. In total, 850,000 galaxies were inserted, but not more than 500 per NIRCcam module at a time to prevent crowding of simulated sources. These images were then analyzed using the same detection and segmentation process, followed by the sample selection criteria of equation 1. As in C. J. Willott et al. (2024), it is found that $\sim 10\%$ of bright objects are not recovered due to overlap with existing galaxies in the images.

Figure 2 shows the completeness of our high- z galaxy selection in the M_{UV} vs. redshift plane. Our selection is $\sim 50\%$ complete down to $M_{\text{UV}} \sim -18.7$ at $z \gtrsim 10$. The observed M_{UV} and redshift values of our high- z sample are also plotted in the figure (yellow points). The distribution of observed galaxies agrees well with the predicted completeness from the simulation (e.g., only a few galaxies in the $< 50\%$ complete area), which supports the validity of our simulation configuration. In particular, if we were to use the original size- M_{UV} relation of T. Morishita et al. (2024) in the simulation, five of the eight galaxies in our sample would be located in the $< 50\%$ completeness region in the $M_{\text{UV}}-z$ plane.

4. RESULTS

4.1. Evolving UV Luminosity Functions

Knowing the completeness of our survey and high- z galaxy selection, we can compute the UV luminosity function and its redshift evolution at $z \gtrsim 10$. Although our selection is nearly complete down to $M_{\text{UV}} \sim -19$ mag beyond $z = 12$, there is only one galaxy found in the total $\sim 23 \text{ arcmin}^2$ unmasked area at $z > 12$, which suggests a significant evolution of the galaxy UV luminosity function at these redshifts. We parameterize the UV LF in an analytical form with redshift-dependent parameters, and directly fit to data without binning in redshift or magnitude to avoid any effect by binning, considering the paucity of $z \gtrsim 11$ galaxies. We adopt the Schechter form (P. Schechter 1976) for the LF,

$$\begin{aligned} \phi_{\text{UV}}(M_{\text{UV}}, z) &= \frac{\ln(10)}{2.5} \phi_{\star}(z) 10^{0.4(\alpha+1)(M_{\text{UV}}^{\star}-M_{\text{UV}})} \exp \left[-10^{0.4(M_{\text{UV}}^{\star}-M_{\text{UV}})} \right], \end{aligned} \quad (2)$$

where α and M_{UV}^{\star} are the faint-end slope and the characteristic UV absolute magnitude, respectively, and $\phi_{\star}(z)$ is the redshift-dependent normalization parameter. We assume a simple redshift dependency, as done by B. Robertson et al. (2024),

$$\log_{10} \phi_{\star}(z) = \log_{10} \phi_{\star,0} + \eta (z - z_0), \quad (3)$$

to reduce the free parameters in the fit. The reference redshift z_0 is fixed to $z_0 = 10$ throughout the paper unless otherwise specified. We also fix α and M_{UV}^{\star} to $\alpha = -2.1$ and $M_{\text{UV}}^{\star} = -21.0$ mag referring to previous studies of UV LFs at $z > 10$ (e.g., N. J. Adams et al. 2024; C. T. Donnan et al. 2024; B. Robertson et al. 2024; C. J. Willott et al. 2024). Thus the model LF has two free parameters of $\phi_{\star,0}$ and η .

We follow H. L. Marshall et al. (1983) for the LF parameter fitting, so that we can also take into account the non-detections in the relatively bright (brighter than $M_{\text{UV}} \sim -19$ mag) galaxies at $z \gtrsim 12$. We derive the best estimations of $\phi_{\star,0}$ and η to minimize the function $S = -2 \ln \mathcal{L}$, where \mathcal{L} is the likelihood and

$$\begin{aligned} \ln \mathcal{L} = & \sum_i^N [\phi_{\text{UV}}(M_{\text{UV},i}, z_i) p(M_{\text{UV},i}, z_i)] \\ & - \iint \phi_{\text{UV}}(M_{\text{UV}}, z) p(M_{\text{UV}}, z) \frac{dV}{dz} dz dM_{\text{UV}}. \end{aligned} \quad (4)$$

The first term is summed over all observed high- z sample galaxies i , and the second term is the integral over all possible range of M_{UV} and z . $p(M_{\text{UV}}, z)$ is the completeness at the point of (M_{UV}, z) , as estimated in

Table 3. Parameters of redshift-dependent Schechter UV LFs at $z > 9.5$ inferred from CANUCS+TEC data.

Parameter	Prior	Posterior
$\log_{10}(\phi_{*,0}/\text{Mpc}^{-3} \text{ mag}^{-1})$	$\mathcal{U}(-8, -2)$	$-4.89^{+0.17}_{-0.20}$
η	$\mathcal{U}(-3, 3)$	$-0.21^{+0.11}_{-0.12}$
α	...	-2.1^*
$M_{\text{UV}}^*/\text{mag}$...	-21.0^*

Notes. The normalization parameter ϕ_* is assumed to evolve depending on redshifts as $\log_{10} \phi_*(z) = \log_{10}(\phi_{*,0}) + \eta(z - 10)$, and the fitting results for the two parameters η and $\log_{10}(\phi_{*,0})$ are given. Values with an asterisk are fixed in the fit.

Sec. 3.2, and dV/dz is the differential volume element at z . The combination of $p(M_{\text{UV}}, z)$ and dV/dz can thus consider the effective sky area of all three fields at (M_{UV}, z) , taking account for the completeness. We use a python implementation of the MCMC (`emcee`; D. Foreman-Mackey et al. 2013) to obtain the posterior distributions of $\phi_{*,0}$ and η , assuming flat priors between $-8 < \log_{10} \phi_{*,0} < -2$ and $-3 < \eta < 3$. Table 3 present the fitting results. The best estimations are from the median of the marginalized posterior distribution, and the uncertainties are from 16th- and 84th-percentiles of the posterior. We here stress again that the fit is based on all redshift ranges where the completeness has non-negligible value and also accounts for the non-detections of galaxies in the $M_{\text{UV}}-z$ plane.

The log-linear rate of the UV LF redshift evolution η obtained in this work ($\eta = -0.21^{+0.11}_{-0.12}$) is consistent with previous work in the JOF that used a similarly rich NIRCcam MB+BB filter set (B. Robertson et al. 2024). This means that the logarithmic galaxy abundance declines at a rate of -0.21 per unit redshift at $z \gtrsim 10$; for example, the number density should decrease by a factor of ~ 7 from $z \sim 11$ to $z \sim 15$. On the other hand, the normalization parameter at the reference redshift $\phi_{*,0}$ in this work is smaller than B. Robertson et al. (2024) by a factor of ~ 0.6 dex (after correcting the difference in the reference redshift z_0 and degeneracy between $\phi_{*,0}$ and M_{UV}^*). This implies that cosmic variance (CV) can significantly affect galaxy number density measurement by at least 0.6 dex.

4.2. Binned UV LFs

Although we estimate the evolving UV LFs without binning the sample galaxies in the previous section, deriving the binned LFs is still useful to compare with LF

Table 4. Binned UV LFs

M_{UV} bin		$\langle M_{\text{UV}} \rangle$	Φ
lower	upper		$10^{-5} \text{ Mpc}^{-3} \text{ mag}^{-1}$
Redshift bin: $9.5 < z < 12$			
-21.0	-20.0	...	< 2.46
-20.0	-19.0	-19.38	$5.97^{+4.72}_{-2.86}$
-19.0	-18.0	-18.75	$11.8^{+11.5}_{-6.4}$
Redshift bin: $12 < z < 16$			
-21.0	-20.0	...	< 1.93
-20.0	-19.0	...	< 2.18
-19.0	-18.0	-18.98	$5.63^{+12.96}_{-4.66}$

Notes. Upper limits are 1σ .

measurements in literature. We use the binned $1/V_a$ method of Y. Avni & J. N. Bahcall (1980) and obtain the LFs at $9.5 < z < 12$ and $12 < z < 16$ separately. The available effective volume for a galaxy i in a redshift/magnitude bin with the size of Δz and ΔM_{UV} is

$$V_a^i = \iint p(M_{\text{UV}}, z) \frac{dV}{dz} dz dM_{\text{UV}}, \quad (5)$$

considering the effect of selection completeness. The LF in the bin is then computed as

$$\Phi = \sum_i^N \frac{1}{V_a^i} \frac{1}{\Delta M_{\text{UV}}} \text{Mpc}^{-3} \text{mag}^{-1}. \quad (6)$$

Uncertainties on the number density is based on Poisson statistics with the correction for small numbers by N. Gehrels (1986).

Table 4 and Figure 3 presents the result. We quote the 1σ upper limits when no galaxy is detected in a bin. In the figure, we also show the marginalized LFs at $z = 10.5$ and $z = 14$ obtained from the MCMC sampling in Sec. 4.1 (black solid curves with red shaded regions). In the lower redshift bin at $z \sim 11$ (left panel in Figure 3), our LF measurements are consistent with or at the lower envelope of other recent JWST studies (P. G. Pérez-González et al. 2023; N. J. Adams et al. 2024; C. T. Donnan et al. 2024; B. Robertson et al. 2024; C. J. Willott et al. 2024; L. Whitler et al. 2025). The spread of LF measurements across the literature is roughly ~ 0.6 dex, which can be understood as the effect of the CV. In the higher redshift bin at $z \sim 14$ (right panel in the figure), although we have only one detection in the faintest magnitude bin, the non-detection of relatively bright ($M_{\text{UV}} < -19$ mag) galaxies in the fairly large survey volume puts a tight constraint on the UV

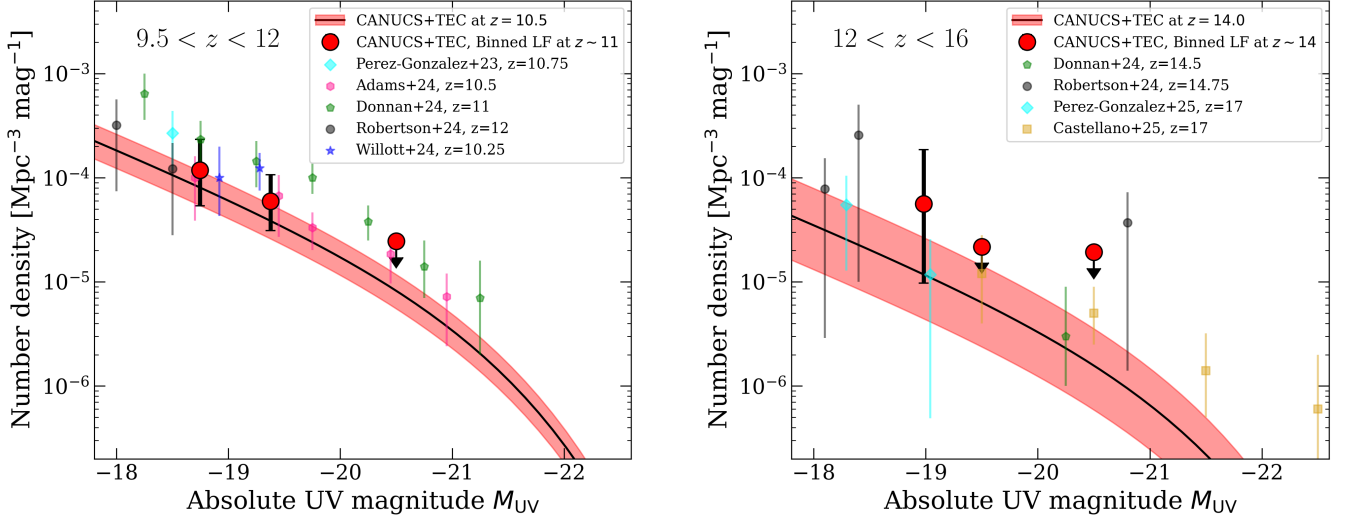


Figure 3. The UV LFs at $z \sim 11$ (left) and $z \sim 14$ (right) from CANUCS+TEC data. Black solid curve is the best estimation of the redshift-evolving UV LF obtained in Sec. 4.1 at $z = 10.5$ (left) and $z = 14$ (right), with the red-shaded area showing 16th- to 84th-percentile. Red filled circles with black error bars present the binned UV LFs in the $9.5 < z < 12$ bin (left) and $12 < z < 16$ bin (right) measured in Sec. 4.2. UV LF measurements in literature at similar redshifts are also shown for comparison (P. G. Pérez-González et al. 2023; N. J. Adams et al. 2024; C. T. Donnan et al. 2024; B. Robertson et al. 2024; C. J. Willott et al. 2024; P. G. Pérez-González et al. 2025; M. Castellano et al. 2025).

LFs, which results in a decline of galaxy abundance at $z > 12$ ($\eta = -0.2$ as obtained in Sec. 4.1). We note that our LF measurement at $z \sim 14$ is comparable to or even lower than recent reports of UV LFs at $z \sim 17$ (M. Castellano et al. 2025; P. G. Pérez-González et al. 2025), which mostly used only NIRCcam BB data to select high- z galaxy candidates. This is possibly due to the low- z interloper contaminants when selecting high- z candidates only based on BB-only catalogs, rather than the effect of CV or very shallow UV LF evolution at $z > 15$ (see Sec. 5.2).

4.3. Cosmic UV Luminosity Density

Given the parameterized UV LF are measured as a function of redshift directly from the data in Sec. 4.1, we can directly compute the redshift evolution of UV luminosity density ($\rho_{UV}(z)$) from the UV LF measurement. We integrate the LF in the Schechter functional form (Eqn. 2) down to $M_{UV} = -17$ mag, and obtain the marginalized $\rho_{UV}(z)$ estimation from the MCMC sampling in Sec. 4.1. Figure 4 shows the median estimation (black solid) with the 16th-84th percentile (red shaded) from our results, comparing with the literature (P. G. Pérez-González et al. 2023, 2025; N. J. Adams et al. 2024; C. T. Donnan et al. 2024; B. Robertson et al. 2024; C. J. Willott et al. 2024; Y. Harikane et al. 2025). The overall ρ_{UV} value in this work is somewhat lower than most JWST studies, and in line with N. J. Adams et al. (2024) and C. J. Willott et al. (2024). Some literature claims that significant modifications of dust, IMF, or

star formation efficiencies (SFEs) in model assumptions are required based on the overabundance of UV bright galaxies at $z > 10$ (e.g., S. L. Finkelstein et al. 2024; Y. Harikane et al. 2025; P. G. Pérez-González et al. 2025). However, our result together with N. J. Adams et al. (2024) and C. J. Willott et al. (2024) should suggest that such significant modifications are not necessarily required.

The log-linear rate of the UV LF evolution η is directly connected to the $\rho_{UV}(z)$ redshift evolution, and our result indicates $\rho_{UV}(z)$ decline as $d \log(\rho_{UV})/dz = -0.21^{+0.11}_{-0.12}$ at $10 < z < 16$. This is less steep than measurements at $z \sim 8 - 11$ by N. J. Adams et al. (2024); C. J. Willott et al. (2024) and consistent with B. Robertson et al. (2024) at $z = 11 - 16$. Importantly, this is also less steep than the prediction by the simple constant extrapolation of the SFE from lower redshift (e.g., Y. Harikane et al. 2022, the gray dash-dot line in Figure 4). These results suggest ρ_{UV} evolution gets shallower above $z \sim 11$, and one of the possible interpretations is the SFE may start to deviate at $z > 11$ from the simple constant extrapolation from lower redshift.

Figure 4 also compares observations to predictions by several simulations: THESAN-ZOOM (R. Kannan et al. 2025), Universe Machine (P. Behroozi et al. 2020), FLARES (A. P. Vijayan et al. 2021; S. M. Wilkins et al. 2023), and SC SAM (L. Y. A. Yung et al. 2024). Simulations are well converged up to $z \sim 8$ but their predictions spread at $z > 8$. However, observational constraints are also scattered at $z > 10$, and it is thus still difficult to

decisively conclude one physical model is favored over others. The large scatter at $z > 10$ in observational data points seems not only due to the Poisson error on small sample size but also to the higher CVs and/or low- z interloper contamination, which will be discussed further in the following section.

5. WHAT CAN BIAS OUR VIEWS OF EARLIEST GALAXY EVOLUTION

5.1. Cosmic variance

A component of observational uncertainty in measuring the high- z galaxy abundance is the CV (e.g., C. L. Steinhardt et al. 2021; G. Desprez et al. 2024; C. J. Willott et al. 2024; C. K. Jespersen et al. 2025). As shown in Sec. 4.1 and 4.3, UV LFs and ρ_{UV} measurements in our CANUCS+TEC fields are ~ 0.6 dex lower than in the JOF by B. Robertson et al. (2024), which can be interpreted as the effect of Poisson + CV uncertainties.

The effect of CV appears larger than nominal predictions based on semi-analytical simulations. There are nine galaxies found at $11.5 < z < 16$ in the JOF, and the predicted uncertainty due to CV on the JOF number count is 23 % (1-sigma), slightly smaller than the Poisson uncertainty (M. Trenti & M. Stiavelli 2008). The combined fractional error would be 41 %, which leads to ~ 0.2 dex uncertainty in the number density estimation including UV LFs, though, our observation shows galaxy abundance measurements can actually be affected by as much as 0.6 dex at this high redshift. Galaxy number statistics at high redshift can thus be considerably affected by field-to-field variance, more severely than the nominal semi-analytical models' predictions, which is presumably due to bursty star-formation (e.g., G. Sun et al. 2023) or non-universal IMFs (e.g., L. Y. A. Yung et al. 2024) in the early universe that can enhance the field-to-field variance. Therefore, building a larger sample of robust high- z galaxies over wide areas in multiple lines of sight is essential to ascertain the earliest galaxy evolution at $z > 10$.

5.2. Low- z interlopers when selecting $z \gtrsim 10$ galaxies only with Broad Bands

Another potential bias is due to low- z interlopers, particularly when selecting $z \gtrsim 10$ galaxies based on BB-only data. To explore this effect, we make a degraded photometry catalog with all MB filters removed except for F410M (hereafter, the BB-only catalog). This catalog contains the HST/ACS F435W, F606W, F814W, and JWST/NIRCam F070W, F090W, F115W, F150W, F200W, F277W, F356W, F410M and F444W filters, and we compare our original results with this catalog. We

run EAZY on this BB-only catalog with exactly the same configuration as in Sec. 2.2, and select high- z galaxies from the same criteria (1).

The BB-only catalog selection high- z sample consists of 10 galaxies, four of them are common with our main high- z sample from the full MB+BB photometry (Sec. 3), while six of them are not. The six galaxies are selected as high- z when only BB filter photometry is available, but turn out to be lower- z with the full MB+BB data ("False Positives"). The False Positives, except for CANUCS-2225353, appear as good-looking dropouts with negligible low- z solution probability (less than ~ 5 %) when the BB-only catalog is used, so it seems inevitable to select them as high- z from BB-only selection (see Appendix A for details of the False Positives). CANUCS-2225353 does pass all selection criteria using the BB-only catalog and is selected as a $z \sim 16$ candidate with F200W-dropout, but the source is also detected in F150W (which is not included as a "blue" filter in the criteria). In the following computation of the BB-only UV LF, we therefore exclude CANUCS-2225353 and use the remaining nine galaxies as the *high- z sample* from the BB-only catalog. The comparison of the BB-only selection high- z sample with our main high- z sample indicates that as much as half of $z \gtrsim 10$ galaxy candidates could actually be low- z interlopers when only BB photometry is available. Of course this fraction largely depends on the selection criteria, data quality (e.g. depth), or observation line of sights (not only clustering of $z > 10$ galaxies but also lower- z interloper clustering can affect this fraction), but this fraction is roughly consistent with simulations using mock galaxy catalogs by N. J. Adams et al. (2025). Thus the low- z interloper contamination is not negligible, particularly at $z \gtrsim 10$ when only BB photometry data is available.

The main population of low- z interlopers in the BB-only selection high- z sample is (very) dusty extreme emission line galaxies (EELGs) at $z > 2$. They typically show large emission line excesses due to [OIII]4959/5007+H β and H α lines on a red continuum at rest optical wavelengths, while being completely undetected in the rest UV at $\lambda_{\text{rest}} \lesssim 3000$ Å, which makes their BB SEDs look as if they are $z > 10$ galaxies (see; e.g., Figure 9, 10, 11, and 12 in Appendix A). Their rest UV light is tremendously attenuated by dust, while the nebular emission lines are not and reaching the equivalent width of $EW_0 \sim 2000$ Å. Some of these extremely reddened EELGs are spectroscopically confirmed in their rest-optical emission lines (e.g., S. Withers et al. 2023; L. Bisigello et al. 2025), but their rest UV properties are almost unknown and there is no good template to replicate the extreme population. The lack of

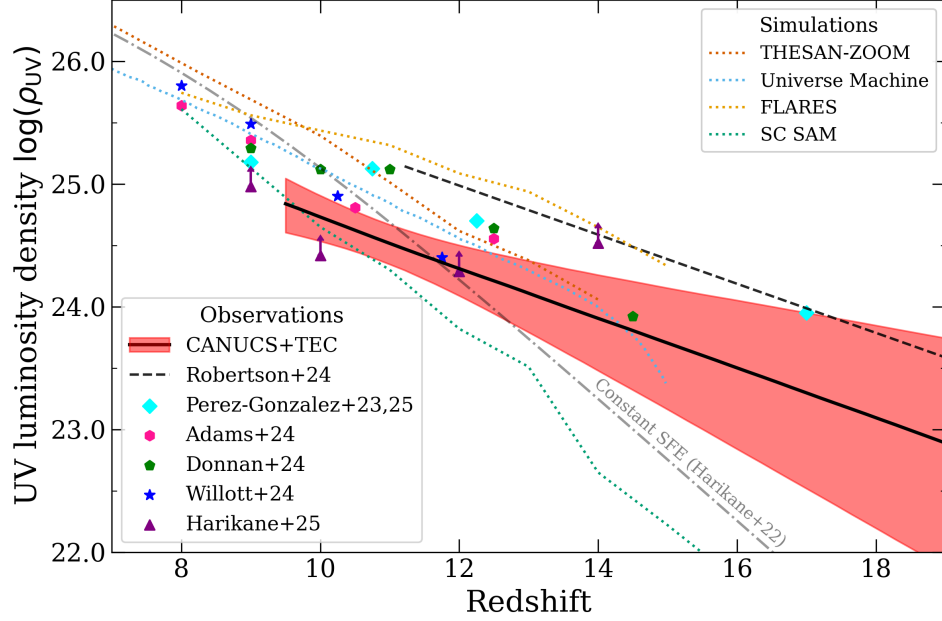


Figure 4. The redshift evolution of cosmic UV luminosity density. Black solid line is the median estimation from CANUCS+TEC data in this work, based on the redshift-evolving UV LF measurement in Sec. 4.1, and red shaded area shows the 16th- to 84th-percentile range. Black dashed line is the ρ_{UV} measurement from JOF observation (B. Robertson et al. 2024), which uses similarly rich NIRCcam MB+BB filters in high- z galaxy selection. For comparison, literature ρ_{UV} measurements from other JWST observations are shown filled small symbols (P. G. Pérez-González et al. 2023; N. J. Adams et al. 2024; C. T. Donnan et al. 2024; C. J. Willott et al. 2024; Y. Harikane et al. 2025). Gray dash-dot curve marks the prediction of ρ_{UV} evolution assuming a constant star-formation efficiency at $z > 6$ by Y. Harikane et al. (2022). Dotted curves present predictions by several theoretical simulations (THESAN-ZOOM, R. Kannan et al. 2025; Universe Machine, P. Behroozi et al. 2020; FLARES, A. P. Vijayan et al. 2021; S. M. Wilkins et al. 2023; SC SAM, L. Y. A. Yung et al. 2024). The ρ_{UV} evolution slope in our work at $z \gtrsim 10$ (black solid line) is somewhat less steep than previous measurements at $z \sim 8$ and in a great agreement with that from JOF data, and starts to deviate from the constant SFE prediction above $z \sim 11$.

good templates results in poor fits with low- z solutions but rather the SED is well-fitted by blue, high- z solutions, when only BB data are available. However with MB observations, the emission lines are clearly identified by the MB flux excesses which strongly supports the low- z solution, and the observed SED is best-fitted with a low- z template although the rest UV non-detection is poorly fitted.

We then investigate the effect of the low- z interloper contaminants on the UV LF measurements. We follow the same procedure as Sec. 4 on the BB-only catalog selection high- z sample and derive the best estimate UV LF redshift evolution from it. In this BB-only UV LF measurement, we also perform the simulation as we do in Sec. 3.2 with removing the MBs to obtain the completeness of the BB-only catalog selection of $9.5 < z < 16$ galaxies. The completeness gets lower in general with the BB-only catalog selection as compared to the standard high- z selection with MB+BBs.

Figure 5 compares the estimated $\phi_*(z)$ evolution from the main high- z galaxy sample (Sec. 4.1) and that from the BB-only UV LF measurement. The overestima-

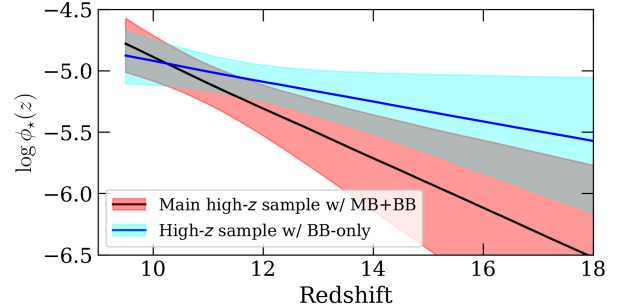


Figure 5. The effect of low- z interlopers on UV LF measurement. Compared is the redshift evolution of $\phi_*(z)$, obtained from the main high- z sample selected with the full MB+BB (red) and from high- z candidates based on BB-only degraded catalog (blue). When building high- z galaxy sample from BB-only catalog, the low- z interlopers can result in ~ 0.6 dex overestimation of galaxy abundance at $z \gtrsim 10$.

tion of the UV LF normalization parameter is severe at higher redshift and it reaches up to ~ 0.6 dex at $z \sim 15$. The overestimation of $\phi_*(z)$ similarly affects the $\rho_{UV}(z)$ measurement. The effect of low- z interlopers is particularly critical at $z \gtrsim 15$, because the galaxy abundance at

$z \gtrsim 15$ becomes very low while the corresponding lower- z range of the interlopers enters intermediate- z range of $z \sim 4$, where extreme line emitters start to commonly populate (e.g., S. Withers et al. 2023; D. J. Eisenstein et al. 2023). Indeed, the two brightest galaxy candidates in the BB-only catalog selection are both False Positive misidentified as $z \sim 16$ galaxies brighter than $M_{UV} = -20$ mag, similar to CEERS-9331 (P. Arrabal Haro et al. 2023). Low- z interlopers can thus bias the UV LF and UV luminosity density measurements by ~ 0.6 dex in BB-only studies. The brighter magnitude bins at higher- z are more likely to be contaminated, and thus LF bright-end studies at $z \gtrsim 10$ need particular caution.

5.3. Effects of interlopers on other galaxy statistics

The considerable contamination by low- z interlopers in the $z \gtrsim 10$ galaxy sample from the BB-only catalog raises caution not only in UV LFs but also in other statistical studies of earliest galaxy properties. In the following, we compare the False Positives and the robust high- z galaxies identified with MB+BB observations in several aspects to reveal the potential effects of low- z interloper contamination in high- z galaxy studies at $z \gtrsim 10$. We here also utilize the JOF $z > 10$ galaxy sample (B. Robertson et al. 2024) as an additional robust high- z galaxy sample, since they select the sample based on similarly rich NIRCcam MB+BB filters. The median redshift of CANUCS+TEC+JOF sample is $\langle z \rangle = 11.5$.

5.3.1. Size- M_{UV} relation

The size- M_{UV} relation is one of the key scaling relations of galaxies and it is an *a priori* assumption in deriving the completeness for the galaxy luminosity function. Figure 6 shows the distribution of the robust high- z galaxy sample from MB+BB data in the size- M_{UV} plane (red squares and black crosses; main sample in this work and from B. Robertson et al. 2024, respectively). The robust high- z galaxy sample distribution is systematically smaller than the size- M_{UV} relation at $11 < z < 13$ previously calibrated by T. Morishita et al. (2024, black line in the figure; the shaded area presents the 1.5-sigma scatter). This systematic offset cannot be fully explained solely by incompleteness: our sample is 50% complete up to $\log(R_{\text{eff}}/\text{kpc}) \sim -0.5$ at $M_{UV} = -19.0$ mag (gray dashed line in the figure), which corresponds to the size- M_{UV} relation median of T. Morishita et al. (2024), while almost all the robust high- z galaxy sample lies well below the T. Morishita et al. (2024) relation. The systematic offset is $\Delta \log(R_{\text{eff}}) = -0.6$ dex (red line in the bottom panel). On the other hand, if we measure the size and absolute

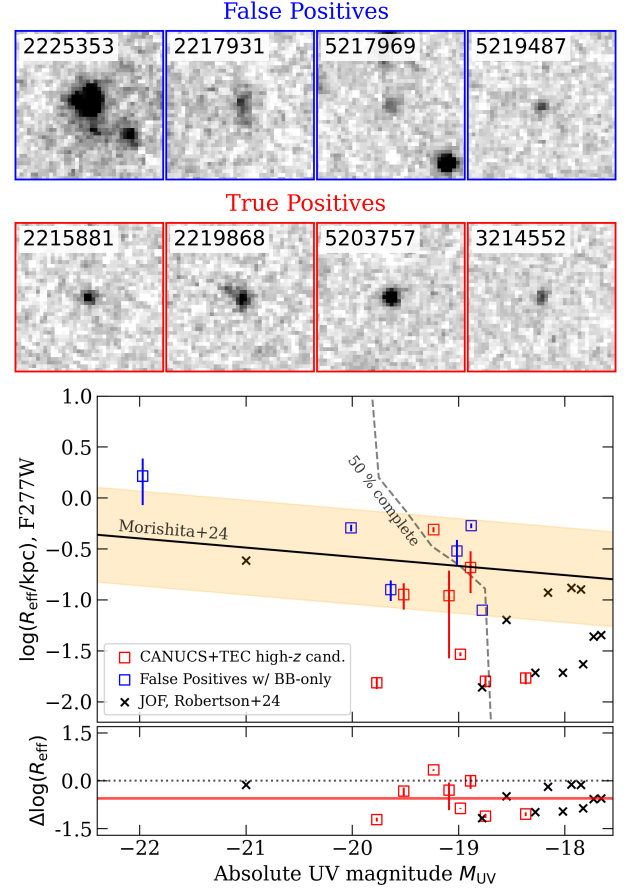


Figure 6. *Top:* cutouts of four examples of False Positives in the F277W filter. They are $1''.6$ on the side. *Middle:* cutouts of four True Positives in the F277W filter. *Bottom:* distribution of high- z galaxy candidates in the size- M_{UV} plane. High- z candidates selected with extensive MB+BB filters (red squares, this work; black crosses, JOF) are systematically smaller than a previous calibration of the size- M_{UV} relation at $z \sim 12$ by T. Morishita et al. (2024, black solid line). On the other hand, the False Positives (blue squares) appear systematically larger than the main high- z and JOF candidates and would align well with the size- M_{UV} relation by T. Morishita et al. (2024). The bottom sub-panel shows the systematic offset in $\log(R_{\text{eff}})$ of the main high- z candidates from the predicted size by T. Morishita et al. (2024) relation. The median offset is -0.6 dex (red line).

UV magnitude of the False Positives based on the BB-only photometry catalog and photo- z estimation from the BB-only data, they distribute very well along the previously calibrated relation (blue squares). Figure 6 thus demonstrates that the False Positives typically appear larger and brighter than the real high- z galaxies, and the size- M_{UV} relation can be biased towards larger sizes when selecting high- z candidates based on BB-only data. In the completeness simulation (Sec. 3.2), we thus assume a modified size- M_{UV} relation of T. Morishita

et al. (2024) offset 0.6 dex smaller. The good agreement between the estimated completeness with this modification and the observed high- z galaxies in the M_{UV} - z plane validates this offset.

5.3.2. Rest UV slopes

Previous JWST studies have found rest-UV slopes, β_{UV} , are blue at the highest redshifts (e.g., F. Cullen et al. 2024; M. W. Topping et al. 2024), and some of them suggest galaxies at $z > 10$ are remarkably blue and could be completely dust-free (F. Cullen et al. 2024). On the other hand, galaxies selected from our CANUCS+TEC data and from JOF (B. Robertson et al. 2024) are typically less blue ($\langle\beta_{UV}\rangle = -2.2$ in CANUCS+TEC and $\langle\beta_{UV}\rangle = -2.5$ in JOF; see also N. Martis et al. 2025 for the high- z red galaxy population in CANUCS+TEC fields). This could indicate that rest-UV slope studies can also be biased in some cases with BB-only data due to bluer galaxies being easier to distinguish from low- z interlopers and to fewer filters to compute β_{UV} .

Figure 7 shows the distribution of the robust high- z sample (CANUCS+TEC, red squares; JOF, black crosses) in the β_{UV} - M_{UV} plane, compared to the $z \sim 11.5$ galaxy sample from F. Cullen et al. (2024) (light blue circles), which mostly used BB-only photometry data in the sample selection. Interestingly, the high- z galaxies selected with MB+BB data distributes in the relatively less blue and fainter locus in the β_{UV} - M_{UV} plane ($M_{UV} \gtrsim -19$ mag and $\beta_{UV} \gtrsim -2.5$), and this population is absent in the F. Cullen et al. (2024) sample. This can be because relatively red high- z galaxies close to the detection limit of the observation can be degenerate with the low- z Balmer break galaxy solution, particularly when only BB data is available, and they could be missed from high- z selection with BB-only data. A representative example is the relatively red $z \sim 15.4$ galaxy candidate CANUCS-321452 (Sec. 3.1), whose low- z probability is substantial ($P_{BB}(z < 7) = 0.13$) when only BB data is used, but negligible with the full MB+BB data ($P(z < 7) = 0.005$). Therefore, BB-only selection of high- z galaxy candidates can be relatively incomplete for faint and less blue galaxies.

On the contrary, some False Positives can mimic very blue high- z SEDs with $\beta_{UV} < -2.5$. Blue squares in Figure 7 show the locations of False Positives in this diagram, where β_{UV} is computed from the BB-only photometry catalog, assuming the photo- z from the BB-only data. This could suggest that low- z interlopers can bias the sample even bluer when only BB data is available.

Combining these two potential effects, incompleteness for faint and less blue galaxies and contamination of low-

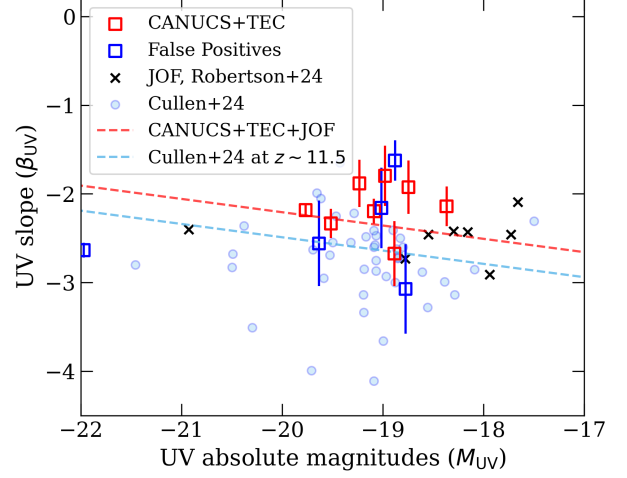


Figure 7. The β_{UV} - M_{UV} relation. High- z galaxy candidates based on MB+BB observations (red squares and black crosses) are less blue than those of a comparison sample mostly based on BB-only data (F. Cullen et al. 2024, cyan circles). In particular, there is a population of faint ($M_{UV} \gtrsim -19$), relatively red ($\beta_{UV} \gtrsim -2.5$) galaxies that is largely absent from the F. Cullen et al. (2024) sample. False Positives (blue squares) cover most of the observed range of β_{UV} . The linear regression of the β_{UV} - M_{UV} relation based on the main MB+BB selection sample (red dashed line) is less blue than found previously (cyan dashed line).

z interlopers that could mimic very blue colors, the β_{UV} - M_{UV} relation can thus be biased bluer with the BB-only data. When only robust MB+BB selection candidates are used (red square and black crosses in Figure 7), the linear regression of the β_{UV} - M_{UV} relation becomes

$$\beta_{UV} = -0.15(M_{UV} + 19) - (2.36 \pm 0.04), \quad (7)$$

fixing the slope $d\beta_{UV}/dM_{UV} = -0.15$ (red dashed line in Figure 7). The intercept of $\beta_{UV}(M_{UV} = -19) = -2.36 \pm 0.04$ at $\langle z \rangle = 11.5$ is redder by $\Delta\beta \sim 0.3$ than F. Cullen et al. (2024, cyan dashed line) at this redshift.

5.4. Future galaxy surveys at $z \gtrsim 10$

By exploiting the robust high- z candidates selected with rich MB+BB data, we demonstrate the importance of MBs in studies of $z \gtrsim 10$ galaxies. However, the number of known galaxies is still small and enlarging the sample size is necessary. The bright-end at $z \gtrsim 14$ needs particular caveats, but bright $z \gtrsim 14$ galaxy candidates are not always interlopers (e.g., GS-z14-0, S. Carniani et al. 2024; K. N. Hainline et al. 2024; MoM-z14, R. P. Naidu et al. 2025). Securing a high- z bright galaxy sample is crucial in various aspects (e.g., bright-end of LFs, scaling relations such as size- M_{UV} relation), and the effect of CV can be considerable in such a rare population search (Sec. 5.1).

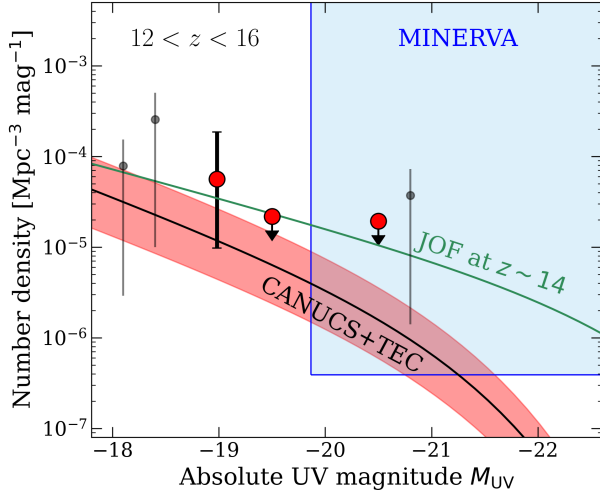


Figure 8. UV LFs at $z \sim 14$ from the two surveys with extensive MB+BB filter observations (CANUCS+TEC, this work; JOF, B. Robertson et al. 2024), compared with the MINERVA survey detectability of $z \sim 14$ galaxies. The two UV LF measurements agree at the faint end ($M_{UV} > -19$) but show a large discrepancy at the bright end. The JWST Cycle 4 MINERVA survey will provide $\sim 500 \text{ arcmin}^2$ with almost all MB+BB filters across four independent line of sights, and will give a tight constraint at the bright end of the highest- z UV LF by building a very robust bright galaxy sample at $z \gtrsim 14$ (blue square area).

Figure 8 compares the UV LF measurements at $z \sim 14$ from this work (black) and from JOF (green; B. Robertson et al. 2024), both are based on MB+BB observations. Although they agree with each other at the faint-end, the bright-end of UV LFs is poorly constrained due to their paucity and the two measurements are largely discrepant at $M_{UV} \lesssim -20 \text{ mag}$. The large discrepant at the bright-end is mainly due to the one presence of one bright galaxy, GS-z14-0, in the small footprint of JOF. The galaxy is thus far the brightest galaxy at this redshift range even across the all JADES field-of-views that covers $\sim \times 15$ area of the JOF, and it can significantly affect the number density of bright galaxies in JOF. It is thus required to search for these bright high- z galaxies with MB+BBs over wide areas in independent lines of sight, mitigating the effect of field-to-field variance.

For example, the MINERVA survey (GO-7814, PI: Muzzin) is scheduled to observe with most MB filters over $\sim 500 \text{ arcmin}^2$ across four independent fields previously observed with the BB set of filters. These observations will give extensive MB+BB filter set observations with $\sim 28 \text{ mag}$ depth over the wide field, and will be able to probe the bright-end of highest- z UV LFs (blue square in Figure 8). The observations are expected to find $N \sim 4$ (in a pessimistic case; the CANUCS+TEC LF) to $N \sim 10$ (optimistic case; the JOF LF) galax-

ies at this redshift brighter than $M_{UV} \lesssim -20 \text{ mag}$, and will give an invaluable sample of bright, high- z galaxies selected with MB+BB observations, like GS-z14-0.

6. SUMMARY

We use the NIRCam Medium-band + Broad-band observations in three independent line-of-sight fields from the combination of the CANUCS program in Cycle 1 and the Technicolor program (TEC) in Cycle 2, to build a robust sample of galaxies at $z > 9.5$ and study the early evolution of the UV LF at $10 \lesssim z \lesssim 16$. The combination of CANUCS+TEC NIRCam observations provides the full set of MB+BB filter images over $\sim 23 \text{ arcmin}^2$ total unmasked area reaching $\sim 29 \text{ mag}$ detection limit. The extensive NIRCam data with all MB+BB filters is useful both in removing low- z interlopers and in selecting faint, relatively red, high- z galaxies. Having MB+BB observations is thus in particular crucial to obtain a robust sample of galaxy candidates at $z > 9.5$, where all strong rest-optical emission lines are redshifted out of the NIRCam wavelength coverage and the Lyman- α continuum break is the only accessible SED feature. We also discuss the potential bias in several aspects of galaxy statistics at $z \gtrsim 10$ due to low- z interlopers when building the sample from BB-only data, by generating a degraded photometry catalog with all MB filters removed from our data and comparing to our main high- z galaxy sample obtained based on the full MB+BB observations.

Our main findings are as follows:

1. We obtain a sample of eight galaxies at $9.5 < z < 16$ with the selection 50 % complete down to $M_{UV} \sim -18.7 \text{ mag}$ over the full redshift range (Figure 2). The highest redshift candidate (CANUCS-3214552) is found at $z_{\text{phot}} \sim 15.4$ with a sharp dropout between F210M and F200W (Figure 1). The galaxy CANUCS-3214552 is faint ($M_{UV} = -19 \text{ mag}$) and relatively red ($\beta = -1.8$), and, due to the relatively red color, it could not be identified as a reliable high- z candidate only with the BB filter data. Also it shows no variability between Cycle 1 and Cycle 2 NIRCam observations, thus CANUCS-3214552 is one of the most reliable candidates of $z > 15$ galaxies, which can be secured only with multi-epoch, full NIRCam MB+BB observations (Sec. 3). It is absolutely necessary to follow-up this galaxy with NIRSpect Prism to confirm its redshift and probe the detailed physical properties.
2. The UV LF from CANUCS+TEC data shows a moderate redshift evolution at $z > 10$. The

- lack of relatively bright galaxies (brighter than $M_{UV} = -20$ mag) and the paucity of $z > 12$ galaxies over ~ 23 arcmin² places tight constraints on the redshift evolution, and the redshift-dependent UV LF normalization parameter is found to be $\log \phi_*(z) = -4.89 - 0.21(z - 10)$ (Table 3 and Figure 3). Our UV LF at $10 < z < 16$ is ~ 0.6 dex lower than a previous work in the JADES Origins Field (JOF), where similarly rich NIRCам MB+BB filters are available, suggesting that the cosmic variance can affect galaxy abundance measurement by at least 0.6 dex in the very high- z universe (Sec. 4.1, 4.2).
3. The UV luminosity density ρ_{UV} measured with CANUCS+TEC observations is at the lower envelope of recent JWST studies and suggests significant modifications of dust, IMF, or star formation efficiencies are not necessarily needed in model assumptions in cosmological simulations (Sec. 4.3).
 4. The log-linear rate of the ρ_{UV} redshift evolution at $z \sim 10 - 16$ from this work is -0.21 . This is somewhat shallower than at lower redshift of $z \sim 8 - 10$ and is consistent with the previous work at the similar redshift in the JOF. Comparing with a prediction of ρ_{UV} evolution assuming the constant star formation efficiency (SFE), it could suggest the SFE starts to deviate from the simple constant extrapolation at $z \gtrsim 11$ (Figure 4 and Sec. 4.3).
 5. By comparing high- z galaxy candidates from the BB-only degraded catalog and from the full MB+BB catalog, the low- z interloper contamination is found to be non-negligible when selecting $z > 9.5$ galaxies based only on the BB data. The major population of interlopers is very dusty EELGs that starts to populate at intermediate redshift of $z > 2$, and roughly a half of $z > 9.5$ galaxy candidates from BB-only photometry could be low- z interlopers (Sec. 5). The most clean galaxy samples at $z \gtrsim 10$ identified from the rich MB+BB observations suggest that highest- z galaxies could be rarer, more compact, and less blue than previously claimed: the UV LF normalization could be overestimated by ~ 0.6 dex when BB-only data is used (Figure 5); the low- z interlopers appears systematically larger than real high- z sources, leading to an overestimation of the size- M_{UV} relation by ~ 0.6 dex (Figure 6); the main high- z galaxy sample from the MB+BB selection is less blue while low- z interlopers can masquerade very blue color in the BB-only SEDs,

resulting in a systematically bluer estimation of the $\beta_{UV} - M_{UV}$ relation by $\Delta\beta \sim -0.3$ (Figure 7).

6. Noteworthy, adding MB observations is effective not only in removing low- z interlopers but also in identifying real high- z candidates that are missed with BB-only selections. Selecting $z \gtrsim 10$ galaxies can be relatively incomplete for faint and less blue galaxies, because their SEDs can be more easily degenerate with low- z Balmer break solutions, particularly when only BB data is available. With MB+BB data, the sharp continuum dropout of the Ly- α break can be captured and the presence of emission lines is strictly ruled out, making low- z solutions prohibited and securing them as reliable high- z candidates (Sec. 5.3.2).

Although we show the significance of the MB observations in obtaining a clean high- z galaxy sample, the number statistics is still small particularly at the bright end of the LF. Enlarging the survey area with NIRCам MB+BB observations is essential to improve our understanding of the earliest galaxy evolution. Future JWST programs scheduled in Cycle 4 such as the MINERVA project will give an invaluable insight (Figure 8).

ACKNOWLEDGMENTS

This work is based on observations made with the NASA/ESA/CSA JWST. The data were obtained from the Mikulski Archive for Space Telescopes at the Space Telescope Science Institute, which is operated by the Association of Universities for Research in Astronomy, Inc., under NASA contract NAS5-03127 for JWST. This research was supported by grants 18JWST-GTO1, 23JWGO2A13, and 23JWGO2B15 from the Canadian Space Agency (CSA), and funding from the Natural Sciences and Engineering Research Council of Canada (NSERC). Support for program JWST-GO-03362 was provided through a grant from the STScI under NASA contract NAS5-03127. This research used the Canadian Advanced Network For Astronomy Research (CANFAR) operated in partnership by the Canadian Astronomy Data Centre and The Digital Research Alliance of Canada with support from the National Research Council of Canada, the Canadian Space Agency, CANARIE and the Canadian Foundation for Innovation. YA is supported by JSPS KAKENHI Grant Number 23H00131. MB, NM, GF, JJ acknowledge support from the ERC Grant FIRSTLIGHT, Slovenian national research agency ARIS through grants N1-0238 and P1-0188, and the program HST-GO-16667, provided through a grant from the STScI under NASA con-

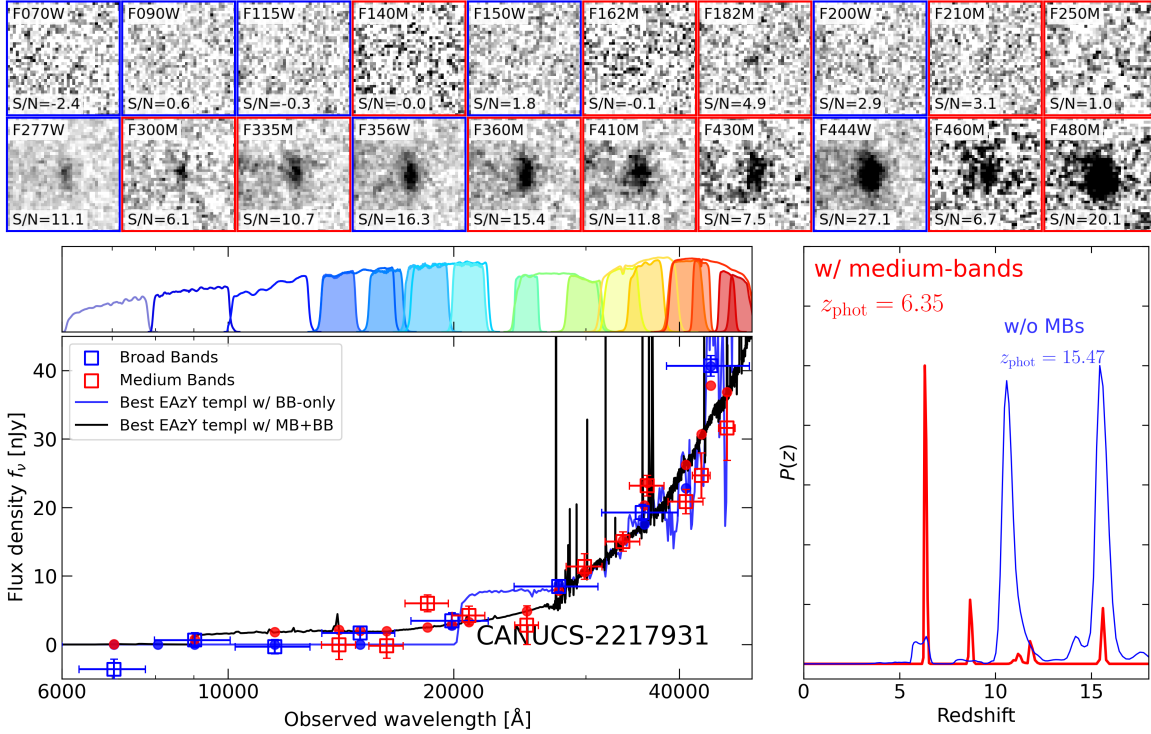


Figure 9. A False Positive CANUCS-2217931. *Top*: cutouts of the source in all NIRCcam images. BB images are displayed with blue frames, while MB images are with red frames. Cutouts are $1''.6$ on the side. *Bottom left*: SED of the source. Photometry in BB and MB filters are shown by blue and red open squares, respectively. The best-fit model spectrum when only BB data are used is shown by blue solid curve, while the best model for all MB+BB data is shown by black. *Bottom right*: $P(z)$ of the source. Blue curve shows the $P(z)$ when only BB data is used, and red shows that for the all MB+BB data SED.

tract NAS5-26555. D.M. and A.L.R. acknowledge support from program JWST-GO-03362, provided through a grant from the STScI under NASA contract NAS5-03127.

Facilities: HST/ACS, JWST/NIRCcam

Software: astropy (Astropy Collaboration et al. 2013, 2018, 2022), EAzy (G. B. Brammer et al. 2008), photutils (L. Bradley et al. 2023), Source Extractor (E. Bertin & S. Arnouts 1996), emcee (D. Foreman-Mackey et al. 2013)

APPENDIX

A. FALSE POSITIVES IN THE BB-ONLY CATALOG SELECTION

This appendix lists the “False Positives” that are selected as $z > 9.5$ in the BB-only catalog but not in the full MB+BB catalog.

A.1. CANUCS-2217931

CANUCS-2217931 is a $z \sim 15$ candidate found in the BB-only catalog with small low- z solution probability (0.0456). The SED shows a break in the F200W-F277W color and is not detected in F070W, F090W, F115W, or F150W filters, which favors $z > 10$ solutions when only BB data is used (blue solid curves in Figure 9). However, with the MB observations, this source shows clear excess in F360M and F480M photometry, and is most likely a very dusty EELG at $z \sim 6$ (black curve in the bottom left).

A.2. CANUCS-2225353

CANUCS-2225353 is a $z \sim 16$ galaxy candidate found in the BB-only catalog with almost zero low- z solution probability (8.1×10^{-5}). The SED shows a clear break in the F200W-F277W color and apparently blue SED from

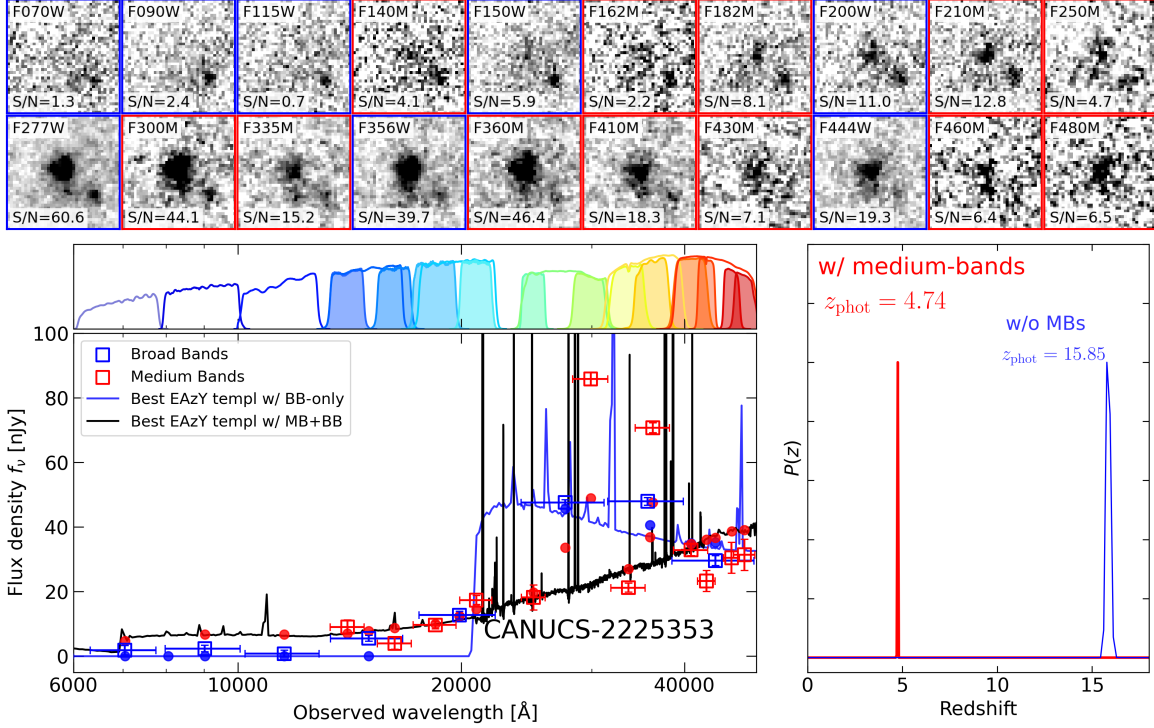


Figure 10. Same as Figure 9 but for CANUCS-2225353.

F277W to F444W, which favors $z \sim 16$ solutions when only BB data is used (blue solid curves in Figure 10). With the MB observations, though, the SED shows extreme excess in F300M and F360M photometry, which clearly indicates the source is a very dusty EELG at $z \sim 5$. The source is detected in F150W with $S/N = 6$, thus CANUCS-2225353 is removed from the *high- z sample* of the BB-only catalog in Section 5.2.

A.3. CANUCS-5217969

CANUCS-5217969 is a $z \sim 12$ candidate found in the BB-only catalog with small low- z solution probability (0.0546). The SED shows a break in the F150W-F200W color and not detected in F070W, F090W, or F115W images. Together with the relatively blue SED from F200W to F444W, the galaxy is identified as a $z \sim 12$ candidate in the BB-only catalog (Figure 11). However, the F182M - F210M color indicates the presence of emission lines at this wavelength, and the MB+BB SED can also be reproduced well with a Balmer break galaxy having emission lines at $z \sim 3$. The MB photometry leads to considerably large low- z probability (0.189).

A.4. CANUCS-5219487

CANUCS-5219487 is a $z \sim 11$ candidate from the BB-only catalog with small low- z solution probability (0.0536). The galaxy is not detected in F070W, F090W, or F115W images, and shows a half drop-out in F150W image, which favors the $z \sim 11$ solution (Figure 12). However with MB observations, the F182M photometry is not bright as the $z \sim 11$ solution predicts, and rather indicates the F200W photometry is boosted by a strong H α emission line at $z \sim 2$.

A.5. CANUCS-3211626 and CANUCS-3211653

CANUCS-3211626 and CANUCS-3211653 are not catastrophic failures in the BB-only photo- z estimation, but their photo- z is slightly lower $\Delta z \sim 0.5 - 1$ with the MB+BB data than BB-only data. The photo- z of CANUCS-3211626 with MB+BB photometry (BB-only photometry) is 9.36 (9.79), and that of CANUCS-3211653 is 9.41 (10.37). They thus are not selected in the MB+BB selection, but are in the BB-only selection. Conversely, there are two galaxies that are selected in the MB+BB selection but not in the BB-only selection, and thus the effect of missing/recovering

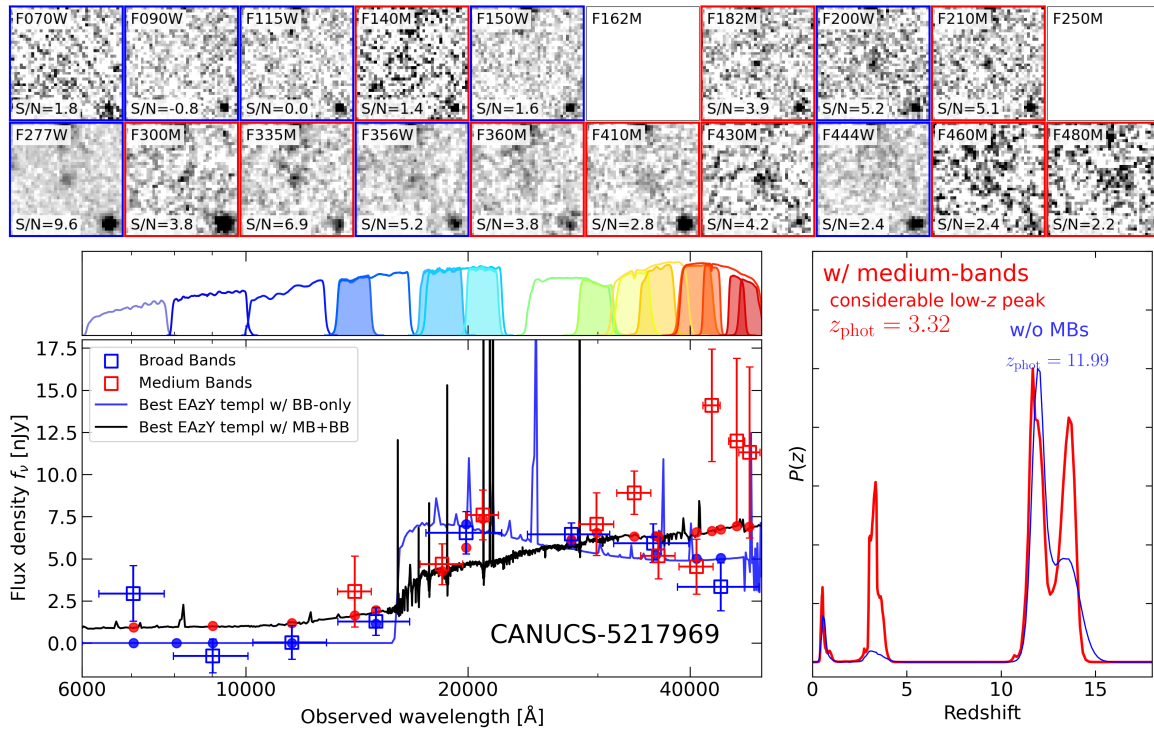


Figure 11. Same as Figure 9 but for CANUCS-5217969.

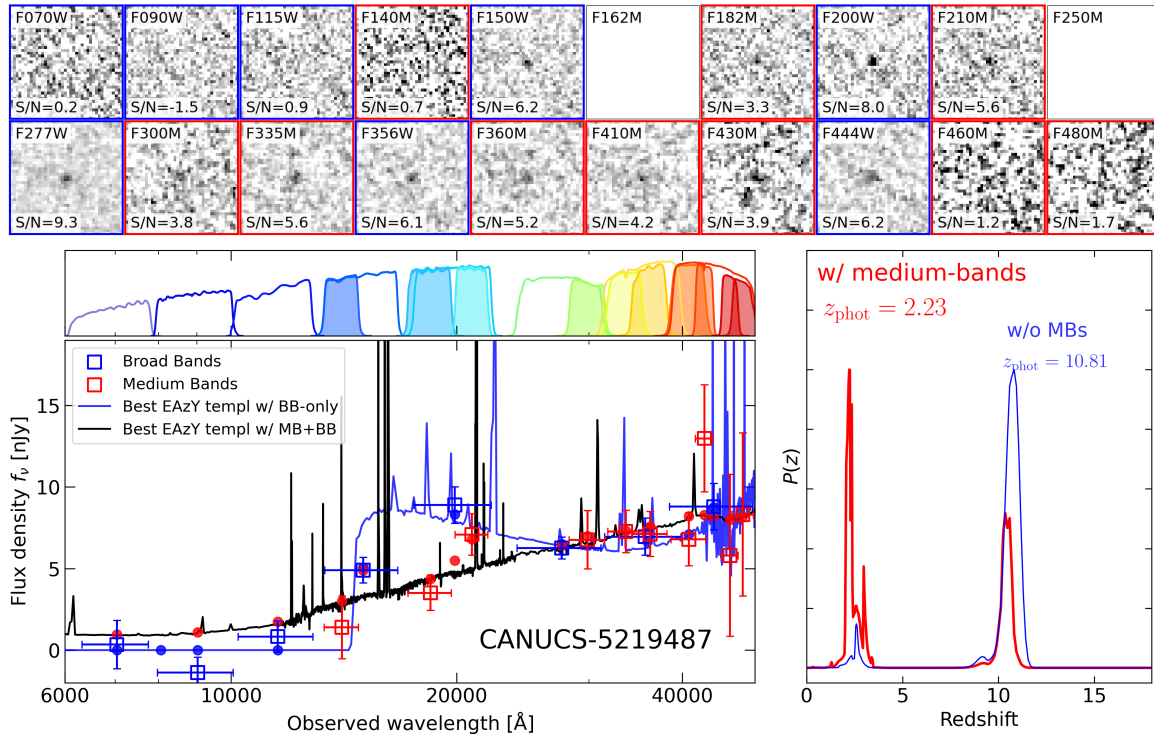


Figure 12. Same as Figure 9 but for CANUCS-5219487.

candidates due to the random errors on photo- z should be negligible in the comparison of the MB+BB selection vs the BB-only selection candidates.

REFERENCES

- Adams, N. J., Conselice, C. J., Austin, D., et al. 2024, *ApJ*, 965, 169, doi: [10.3847/1538-4357/ad2a7b](https://doi.org/10.3847/1538-4357/ad2a7b)
- Adams, N. J., Austin, D., Harvey, T., et al. 2025, arXiv e-prints, arXiv:2502.10282, doi: [10.48550/arXiv.2502.10282](https://doi.org/10.48550/arXiv.2502.10282)
- Arrabal Haro, P., Dickinson, M., Finkelstein, S. L., et al. 2023, *Nature*, 622, 707, doi: [10.1038/s41586-023-06521-7](https://doi.org/10.1038/s41586-023-06521-7)
- Asada, Y., Desprez, G., Willott, C. J., et al. 2025, *ApJL*, 983, L2, doi: [10.3847/2041-8213/adc388](https://doi.org/10.3847/2041-8213/adc388)
- Astropy Collaboration, Robitaille, T. P., Tollerud, E. J., et al. 2013, *A&A*, 558, A33, doi: [10.1051/0004-6361/201322068](https://doi.org/10.1051/0004-6361/201322068)
- Astropy Collaboration, Price-Whelan, A. M., Sipőcz, B. M., et al. 2018, *AJ*, 156, 123, doi: [10.3847/1538-3881/aabc4f](https://doi.org/10.3847/1538-3881/aabc4f)
- Astropy Collaboration, Price-Whelan, A. M., Lim, P. L., et al. 2022, *ApJ*, 935, 167, doi: [10.3847/1538-4357/ac7c74](https://doi.org/10.3847/1538-4357/ac7c74)
- Avni, Y., & Bahcall, J. N. 1980, *ApJ*, 235, 694, doi: [10.1086/157673](https://doi.org/10.1086/157673)
- Behroozi, P., Conroy, C., Wechsler, R. H., et al. 2020, *MNRAS*, 499, 5702, doi: [10.1093/mnras/staa3164](https://doi.org/10.1093/mnras/staa3164)
- Bertin, E., & Arnouts, S. 1996, *A&AS*, 117, 393, doi: [10.1051/aas:1996164](https://doi.org/10.1051/aas:1996164)
- Bisigello, L., Gandolfi, G., Feltre, A., et al. 2025, *A&A*, 693, L18, doi: [10.1051/0004-6361/202452604](https://doi.org/10.1051/0004-6361/202452604)
- Bouwens, R. J., Oesch, P. A., Stefanon, M., et al. 2021, *AJ*, 162, 47, doi: [10.3847/1538-3881/abf83e](https://doi.org/10.3847/1538-3881/abf83e)
- Bradley, L., Sipőcz, B., Robitaille, T., et al. 2023, 1.8.0 Zenodo, doi: [10.5281/zenodo.7946442](https://doi.org/10.5281/zenodo.7946442)
- Brammer, G. B., van Dokkum, P. G., & Coppi, P. 2008, *ApJ*, 686, 1503, doi: [10.1086/591786](https://doi.org/10.1086/591786)
- Carniani, S., Hainline, K., D'Eugenio, F., et al. 2024, *Nature*, 633, 318, doi: [10.1038/s41586-024-07860-9](https://doi.org/10.1038/s41586-024-07860-9)
- Carniani, S., D'Eugenio, F., Ji, X., et al. 2025, *A&A*, 696, A87, doi: [10.1051/0004-6361/202452451](https://doi.org/10.1051/0004-6361/202452451)
- Castellano, M., Fontana, A., Merlin, E., et al. 2025, arXiv e-prints, arXiv:2504.05893, doi: [10.48550/arXiv.2504.05893](https://doi.org/10.48550/arXiv.2504.05893)
- Conroy, C., & Gunn, J. E. 2010, Astrophysics Source Code Library, record ascl:1010.043
- Cullen, F., McLeod, D. J., McLure, R. J., et al. 2024, *MNRAS*, 531, 997, doi: [10.1093/mnras/stae1211](https://doi.org/10.1093/mnras/stae1211)
- DeCoursey, C., Egami, E., Pierel, J. D. R., et al. 2025, *ApJ*, 979, 250, doi: [10.3847/1538-4357/ad8fab](https://doi.org/10.3847/1538-4357/ad8fab)
- Desprez, G., Martis, N. S., Asada, Y., et al. 2024, *MNRAS*, 530, 2935, doi: [10.1093/mnras/stae1084](https://doi.org/10.1093/mnras/stae1084)
- Donnan, C. T., McLeod, D. J., Dunlop, J. S., et al. 2023, *MNRAS*, 518, 6011, doi: [10.1093/mnras/stac3472](https://doi.org/10.1093/mnras/stac3472)
- Donnan, C. T., McLure, R. J., Dunlop, J. S., et al. 2024, *MNRAS*, 533, 3222, doi: [10.1093/mnras/stae2037](https://doi.org/10.1093/mnras/stae2037)
- Eisenstein, D. J., Johnson, B. D., Robertson, B., et al. 2023, arXiv e-prints, arXiv:2310.12340, doi: [10.48550/arXiv.2310.12340](https://doi.org/10.48550/arXiv.2310.12340)
- Finkelstein, S. L., Leung, G. C. K., Bagley, M. B., et al. 2024, *ApJL*, 969, L2, doi: [10.3847/2041-8213/ad4495](https://doi.org/10.3847/2041-8213/ad4495)
- Fitzpatrick, E. L. 1999, *PASP*, 111, 63, doi: [10.1086/316293](https://doi.org/10.1086/316293)
- Foreman-Mackey, D., Hogg, D. W., Lang, D., & Goodman, J. 2013, *PASP*, 125, 306, doi: [10.1086/670067](https://doi.org/10.1086/670067)
- Gehrels, N. 1986, *ApJ*, 303, 336, doi: [10.1086/164079](https://doi.org/10.1086/164079)
- Hainline, K. N., Johnson, B. D., Robertson, B., et al. 2024, *ApJ*, 964, 71, doi: [10.3847/1538-4357/adlee4](https://doi.org/10.3847/1538-4357/adlee4)
- Harikane, Y., Ono, Y., Ouchi, M., et al. 2022, *ApJS*, 259, 20, doi: [10.3847/1538-4365/ac3dfc](https://doi.org/10.3847/1538-4365/ac3dfc)
- Harikane, Y., Ouchi, M., Oguri, M., et al. 2023, *ApJS*, 265, 5, doi: [10.3847/1538-4365/acaaa9](https://doi.org/10.3847/1538-4365/acaaa9)
- Harikane, Y., Inoue, A. K., Ellis, R. S., et al. 2025, *ApJ*, 980, 138, doi: [10.3847/1538-4357/ad9b2c](https://doi.org/10.3847/1538-4357/ad9b2c)
- Inoue, A. K., Shimizu, I., Iwata, I., & Tanaka, M. 2014, *MNRAS*, 442, 1805, doi: [10.1093/mnras/stu936](https://doi.org/10.1093/mnras/stu936)
- Jespersen, C. K., Steinhardt, C. L., Somerville, R. S., & Lovell, C. C. 2025, *ApJ*, 982, 23, doi: [10.3847/1538-4357/adb422](https://doi.org/10.3847/1538-4357/adb422)
- Kannan, R., Puchwein, E., Smith, A., et al. 2025, arXiv e-prints, arXiv:2502.20437, doi: [10.48550/arXiv.2502.20437](https://doi.org/10.48550/arXiv.2502.20437)
- Larson, R. L., Hutchison, T. A., Bagley, M., et al. 2023, *ApJ*, 958, 141, doi: [10.3847/1538-4357/acfed4](https://doi.org/10.3847/1538-4357/acfed4)
- Lotz, J. M., Koekemoer, A., Coe, D., et al. 2017, *ApJ*, 837, 97, doi: [10.3847/1538-4357/837/1/97](https://doi.org/10.3847/1538-4357/837/1/97)
- Marshall, H. L., Tananbaum, H., Avni, Y., & Zamorani, G. 1983, *ApJ*, 269, 35, doi: [10.1086/161016](https://doi.org/10.1086/161016)
- Martis, N., Withers, S., Felicioni, G., et al. 2025, arXiv e-prints, arXiv:2503.01579, doi: [10.48550/arXiv.2503.01579](https://doi.org/10.48550/arXiv.2503.01579)
- Morishita, T., Stiavelli, M., Chary, R.-R., et al. 2024, *ApJ*, 963, 9, doi: [10.3847/1538-4357/ad1404](https://doi.org/10.3847/1538-4357/ad1404)
- Naidu, R. P., Oesch, P. A., Brammer, G., et al. 2025, arXiv e-prints, arXiv:2505.11263, doi: [10.48550/arXiv.2505.11263](https://doi.org/10.48550/arXiv.2505.11263)
- Oke, J. B., & Gunn, J. E. 1983, *ApJ*, 266, 713, doi: [10.1086/160817](https://doi.org/10.1086/160817)

- Peng, C. Y., Ho, L. C., Impey, C. D., & Rix, H.-W. 2010, *AJ*, 139, 2097, doi: [10.1088/0004-6256/139/6/2097](https://doi.org/10.1088/0004-6256/139/6/2097)
- Pérez-González, P. G., Costantin, L., Langeroodi, D., et al. 2023, *ApJL*, 951, L1, doi: [10.3847/2041-8213/acd9d0](https://doi.org/10.3847/2041-8213/acd9d0)
- Pérez-González, P. G., Östlin, G., Costantin, L., et al. 2025, arXiv e-prints, arXiv:2503.15594, doi: [10.48550/arXiv.2503.15594](https://doi.org/10.48550/arXiv.2503.15594)
- Robertson, B., Johnson, B. D., Tacchella, S., et al. 2024, *ApJ*, 970, 31, doi: [10.3847/1538-4357/ad463d](https://doi.org/10.3847/1538-4357/ad463d)
- Sarrouh, G. T. E., Muzzin, A., Iyer, K. G., et al. 2024, *ApJL*, 967, L17, doi: [10.3847/2041-8213/ad43e8](https://doi.org/10.3847/2041-8213/ad43e8)
- Sarrouh, G. T. E., Asada, Y., Martis, N. S., et al. 2025, arXiv e-prints, arXiv:2506.21685, <https://arxiv.org/abs/2506.21685>
- Schechter, P. 1976, *ApJ*, 203, 297, doi: [10.1086/154079](https://doi.org/10.1086/154079)
- Steinhardt, C. L., Jespersen, C. K., & Linzer, N. B. 2021, *ApJ*, 923, 8, doi: [10.3847/1538-4357/ac2a2f](https://doi.org/10.3847/1538-4357/ac2a2f)
- Suess, K. A., Weaver, J. R., Price, S. H., et al. 2024, *ApJ*, 976, 101, doi: [10.3847/1538-4357/ad75fe](https://doi.org/10.3847/1538-4357/ad75fe)
- Sun, G., Faucher-Giguère, C.-A., Hayward, C. C., et al. 2023, *ApJL*, 955, L35, doi: [10.3847/2041-8213/acf85a](https://doi.org/10.3847/2041-8213/acf85a)
- Topping, M. W., Stark, D. P., Endsley, R., et al. 2024, *MNRAS*, 529, 4087, doi: [10.1093/mnras/stae800](https://doi.org/10.1093/mnras/stae800)
- Trenti, M., & Stiavelli, M. 2008, *ApJ*, 676, 767, doi: [10.1086/528674](https://doi.org/10.1086/528674)
- Vijayan, A. P., Lovell, C. C., Wilkins, S. M., et al. 2021, *MNRAS*, 501, 3289, doi: [10.1093/mnras/staa3715](https://doi.org/10.1093/mnras/staa3715)
- Whitler, L., Stark, D. P., Topping, M. W., et al. 2025, arXiv e-prints, arXiv:2501.00984, doi: [10.48550/arXiv.2501.00984](https://doi.org/10.48550/arXiv.2501.00984)
- Wilkins, S. M., Vijayan, A. P., Lovell, C. C., et al. 2023, *MNRAS*, 519, 3118, doi: [10.1093/mnras/stac3280](https://doi.org/10.1093/mnras/stac3280)
- Williams, C. C., Alberts, S., Ji, Z., et al. 2024, *ApJ*, 968, 34, doi: [10.3847/1538-4357/ad3f17](https://doi.org/10.3847/1538-4357/ad3f17)
- Willott, C. J., Doyon, R., Albert, L., et al. 2022, *PASP*, 134, 025002, doi: [10.1088/1538-3873/ac5158](https://doi.org/10.1088/1538-3873/ac5158)
- Willott, C. J., Desprez, G., Asada, Y., et al. 2024, *ApJ*, 966, 74, doi: [10.3847/1538-4357/ad35bc](https://doi.org/10.3847/1538-4357/ad35bc)
- Withers, S., Muzzin, A., Ravindranath, S., et al. 2023, *ApJL*, 958, L14, doi: [10.3847/2041-8213/ad01c0](https://doi.org/10.3847/2041-8213/ad01c0)
- Yan, H., Ma, Z., Sun, B., et al. 2023, *ApJS*, 269, 43, doi: [10.3847/1538-4365/ad0298](https://doi.org/10.3847/1538-4365/ad0298)
- Yung, L. Y. A., Somerville, R. S., Finkelstein, S. L., Wilkins, S. M., & Gardner, J. P. 2024, *MNRAS*, 527, 5929, doi: [10.1093/mnras/stad3484](https://doi.org/10.1093/mnras/stad3484)